



RESEARCH ARTICLE

10.1002/2017JC012910

Testing Munk's hypothesis for submesoscale eddy generation using observations in the North Atlantic

Christian E. Buckingham^{1,2} , Zammath Khaleel^{1,3}, Ayah Lazar^{4,5}, Adrian P. Martin⁶ , John T. Allen^{7,8}, Alberto C. Naveira Garabato¹, Andrew F. Thompson⁴ , and Clément Vic¹

¹National Oceanography Centre, University of Southampton, Southampton, UK, ²Now at British Antarctic Survey, Cambridge, UK, ³Now at Ministry of Environment and Energy, Malé, Maldives, ⁴California Institute of Technology, Pasadena, California, USA, ⁵Now at Israel Oceanographic and Limnological Research, Haifa, Israel, ⁶National Oceanography Centre, Southampton, UK, ⁷University of Portsmouth, Portsmouth, UK, ⁸VECTis Environmental Consultants, LLP, Portsmouth, UK

Key Points:

- A high-resolution satellite image reveals an ocean front populated by submesoscale vortices
- Linear theory applied to coincident hydrography suggests vortices result not from barotropic but baroclinic instability
- This study documents rare observational evidence of submesoscale baroclinic instability in the open ocean

Supporting Information:

- Supporting Information S1

Correspondence to:

C. E. Buckingham,
c.e.buckingham@bas.ac.uk

Citation:

Buckingham, C. E., Z. Khaleel, A. Lazar, A. P. Martin, J. T. Allen, A. C. Naveira Garabato, A. F. Thompson, and C. Vic (2017), Testing Munk's hypothesis for submesoscale eddy generation using observations in the North Atlantic, *J. Geophys. Res. Oceans*, 122, doi:10.1002/2017JC012910.

Received 24 MAR 2017

Accepted 18 JUL 2017

Accepted article online 24 JUL 2017

Abstract A high-resolution satellite image that reveals a train of coherent, submesoscale (6 km) vortices along the edge of an ocean front is examined in concert with hydrographic measurements in an effort to understand formation mechanisms of the submesoscale eddies. The infrared satellite image consists of ocean surface temperatures at ~390 m resolution over the midlatitude North Atlantic (48.69°N, 16.19°W). Concomitant altimetric observations coupled with regular spacing of the eddies suggest the eddies result from mesoscale stirring, filamentation, and subsequent frontal instability. While horizontal shear or barotropic instability (BTI) is one mechanism for generating such eddies (Munk's hypothesis), we conclude from linear theory coupled with the in situ data that mixed layer or submesoscale baroclinic instability (BCI) is a more plausible explanation for the observed submesoscale vortices. Here we assume that the frontal disturbance remains in its linear growth stage and is accurately described by linear dynamics. This result likely has greater applicability to the open ocean, i.e., regions where the gradient Rossby number is reduced relative to its value along coasts and within strong current systems. Given that such waters comprise an appreciable percentage of the ocean surface and that energy and buoyancy fluxes differ under BTI and BCI, this result has wider implications for open-ocean energy/buoyancy budgets and parameterizations within ocean general circulation models. In summary, this work provides rare observational evidence of submesoscale eddy generation by BCI in the open ocean.

Plain Language Summary Here, we test Munk's theory for small-scale eddy generation using a unique set of satellite- and ship-based observations. We find that for one particular set of observations in the North Atlantic, the mechanism for eddy generation is not pure horizontal shear, as proposed by *Munk et al.* (2000) and Munk (2001), but is instead vertical shear, or baroclinic instability. While by itself, this is not a globally important result, taken in the context of mesoscale eddies which are ubiquitous in the World Ocean, this suggests energy exchanges in the more ambient, open ocean are the result of the latter mechanism. In conclusion, submesoscale eddy generation is poorly understood in the ocean and we need to better constrain our geographical and temporal understanding of these processes for representation in coarse-resolution models.

1. Background

Submesoscale processes are believed to play important roles in ocean turbulence, stratification, and primary productivity [Boccaletti et al., 2007; Fox-Kemper et al., 2008a, 2008b; Thomas et al., 2008; Klein and Lapeyre, 2009; Fox-Kemper et al., 2011; Lévy et al., 2012; Mahadevan et al., 2012; Omand et al., 2015; Brüggemann and Eden, 2015; Gula et al., 2016]. Despite this fact, observations of submesoscale phenomena are scarce. Traditional sampling strategies often fail to resolve these phenomena owing to their small-to-moderate lateral scale (0.1–10 km) and quickly evolving nature (hours to days). While expensive field campaigns have been designed to overcome this challenge—examples include the Scalable Lateral Mixing and Coherent Turbulence (i.e., LatMix) [Shcherbina et al., 2015], Ocean Surface Mixing, Ocean Submesoscale Interaction Study (OSMOSIS) [Buckingham et al., 2016; Thompson et al., 2016; Pearson et al., 2015], and Surface Mixed Layer

© 2017. The Authors.

This is an open access article under the terms of the Creative Commons Attribution License, which permits use, distribution and reproduction in any medium, provided the original work is properly cited.

Evolution at Submesoscales (SMILES) experiments—additional observations are needed to validate these model-driven hypotheses.

One approach to overcoming the sampling problem is to use remotely sensed data. Such data offer a solution to this problem by yielding two-dimensional (2-D)—and in the case of repeated measurements in time, three-dimensional (3D)—snapshots of the ocean surface at considerably high resolution. An excellent example of this analysis was provided by the study of an upwelling front in the California Current System [Flament *et al.*, 1985]. Examining repeated satellite infrared (IR) images of an ocean front off the Californian coast, Flament *et al.* [1985] found evidence of submesoscale eddy generation resulting from horizontal shear instability. Another useful example is the analysis of optical imagery collected from the Apollo shuttle missions [Scully-Power, 1986; Munk *et al.*, 2000; Munk, 2001]. These images were collected at high spatial resolution from a hand-held fixed-focal length camera during the 1980s and revealed the existence of submesoscale “spiral eddies”—so-called because of their spiral-like appearance. As postulated by Munk *et al.* [2000], these features result from horizontal shear and the subsequent roll-up of vortices. Moreover, they are visible on the ocean surface as a result of glitter patterns interacting with ocean surfactants. While repeat snapshots were not available from the space shuttle within the required time scale (i.e., hours to several days), the ubiquity of such oceanographic features in the global ocean were not known prior to these observations. McWilliams [1985] provides a nice summary of what was known up until that time. See, also, McWilliams [2016] for a modern-day review of oceanic submesoscale currents.

One question that remains outstanding in the oceanographic community is, “What are the relative roles of horizontal and vertical shear in generating submesoscale vortices in the global ocean?” While we know from analytical and numerical modeling solutions that submesoscale vortices can be generated by both (1) horizontal shear instability (barotropic instability, BTI) [D’Asaro, 1988; Munk *et al.*, 2000; Munk, 2001] and (2) vertical shear (baroclinic instability, BCI) [Samelson, 1993; Haine and Marshall, 1998; Eldevik and Dysthe, 1999, 2002], their relative importance may differ with geographic location and time of year. Furthermore, because the energy sources for these disturbances differ and because BTI has a negligible effect upon upper ocean stratification whereas BCI restratifies the surface ocean [Haine and Marshall, 1998; Boccaletti *et al.*, 2007], the answer to this question has important consequences for energy and buoyancy budgets in the upper ocean. This, in turn, may moderate climate as a result of changes in ocean-atmosphere heat and gas exchange. While such effects might be parameterized on the basis of mesoscale velocity and buoyancy fields and, thus, validated to some degree using satellite altimetry in concert with high-resolution observations, at the moment we have scant high-resolution observations to substantiate such parameterizations.

Recognizing that submesoscale-resolving observations are limited and motivated by the unaddressed question posed above, we proceed to identify satellite imagery coincident with preexisting in situ measurements and search for evidence of submesoscale eddy generation. The study begins over the open ocean in the North Atlantic where in situ data were collected as part of the OSMOSIS field campaign. By systematically identifying cloud-free periods and cross-referencing these with high-resolution IR imagery, we identify a single satellite image revealing coherent, submesoscale vortices on the edge of an ocean front. The image is coincident with a high-resolution hydrographic survey (i.e., from SeaSoar) conducted over the front, from which we can calculate relevant dynamical parameters. We then proceed to examine whether BTI or BCI are most responsible for the observed submesoscale vortices. In light of the submesoscale eddy generation mechanism proposed by Munk *et al.* [2000] and a comment made by Munk in discussing this eddy generation mechanism [Munk, 2001, last paragraph on p. 197], we refer to this as “testing Munk’s hypothesis” that submesoscale eddies are generated by BTI [Munk *et al.*, 2000; Munk, 2001]. We acknowledge we do not have concomitant optical imagery. This also seems fitting as this year marks Dr. Walter Munk’s 100th birthday.

The outline of this study is as follows. In section 2, we describe the methods and data sets used in this study. In section 3, we document the ultra-high-resolution satellite image in which the ocean front is observed. In section 4, we conduct a linear instability analysis of the front and test the hypothesis that pure BTI is responsible for the observed eddies. Noting that horizontal shear does not accurately explain the observed scale of the instability (section 4.3.1), we turn our attention to BCI as an alternative mechanism. The constraints of the BCI model used in this study limit conclusions to some degree. Nevertheless, we demonstrate that BCI

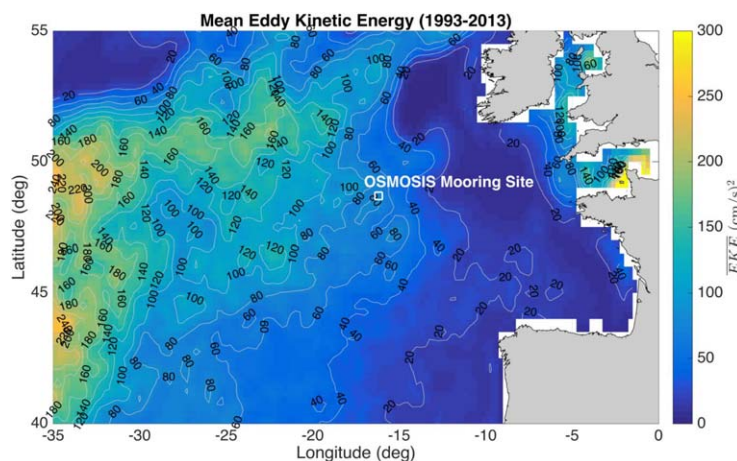


Figure 1. The location of the OSMOSIS mooring site (48.69°N, 16.19°W, September 2012 to September 2013) overlain on mean eddy kinetic energy (EKE). Signatures of the Gulf Stream’s extension into the Atlantic is seen to the west while a more latent eastern boundary current is and continental shelf waters are found to the east. Mean EKE was computed from satellite altimetry (1993–2013).

is a more plausible solution than BTI in explaining the disturbance and the observed submesoscale eddies (section 4.3.2). We summarize conclusions in section 5 and discuss these findings in section 6.

2. Methods

OSMOSIS was a research consortium formed to better understand competing turbulent processes within the ocean surface boundary layer (SBL), including Langmuir turbulence and submesoscale processes. The observational component of the study included two process study

cruises, year-long mooring and year-long glider observations, September 2012 to September 2013, all of which took place in the eastern North Atlantic (48.69°N, 16.19°W, Figure 1) [Allen *et al.*, 2013; Buckingham *et al.*, 2016; Thompson *et al.*, 2016; Damerell *et al.*, 2016]. In order to help with interpretation of these observations, we sought high-resolution satellite imagery throughout the entire year. Remote sensing platforms equipped with optical and synthetic aperture radar (SAR) provide images with sufficient resolution. However, measurements from these platforms were not scheduled prior to the experiment. IR instruments, which yield images at $O(1)$ km pixel resolution, were identified as a possible resource, despite signal attenuation due to atmospheric water vapor.

2.1. Obtaining High-Resolution Satellite Infrared Imagery

It is common for weeks to pass in the North Atlantic before a cloud-free image is obtained, particularly during winter. This was true during the OSMOSIS year-long experiment and necessitates a systematic approach to obtaining IR imagery. While data distribution systems that subset data files at user-specified times and locations can help, not all satellite data are served in this manner. Our approach to overcoming this hurdle was to develop a time series of cloud cover at the OSMOSIS site from geosynchronous (GS) data and cross-reference periods of low cloud cover with available high-resolution imagery from a polar-orbiting (PO) spacecraft. In this study, we made use of thermal imagery from the Visible and Infrared Imaging Radiometer Suite (VIIRS) located on Suomi National Polar-orbiting Partnership (NPP) owing to its ability to resolve fine-scale ocean structure [Khaleel, 2015; Schloesser *et al.*, 2016].

2.1.1. Geosynchronous or Geostationary Satellite Measurements

The Spinning Enhanced Visible and InfraRed Imager (SEVIRI) sensor onboard the Meteosat Second Generation (MSG) spacecraft provides considerable coverage at our location. This spacecraft orbits the Earth at geostationary altitude (i.e., $\sim 36,000$ km), yielding images of the Earth every 15 min. Measurements within different spectral bands are then combined to yield estimates of sea surface temperature (SST) every 30 min at 6 km resolution (8 km at our location) [Maturi *et al.*, 2008]. While the use of model output (e.g., from the European Centre for Medium-Range Weather Forecasting, ECMWF, or National Center for Environmental Prediction, NCEP) was considered, these data have much coarser temporal and spatial resolution when compared with those from GS spacecraft. Additionally, models assimilate measurements from a variety of sources, including those from the microwave portion of the spectrum [Bauer *et al.*, 2010]. These factors provide an argument for the use of observations rather than model data to estimate coverage by clouds.

Fractional cloud cover, $\gamma(R, t)$, is defined as the average number of poor-quality pixels within a circle of radius R centered on the mooring site at time t (i.e., 48.69°N, 16.19°W):

$$\gamma(R, t) = \frac{\sum_{i=1}^m (\text{poor quality pixels})}{\sum_{j=1}^n (\text{total pixels})} \quad (1)$$

Here m is the number of pixels flagged as cloudy using a Bayesian algorithm and included in the data product described below [Maturi et al., 2008; Saunders and Kriebel, 1988; Merchant et al., 2005] and n is the total number of pixels enclosed by the circle. To provide greater understanding of cloud coverage, we computed γ for four small circles (Figure 2a). Our interpretation was that cloud coverage is (a) homogeneous when all four estimates of γ illustrate similar trends and (b) present but inhomogeneous when γ records for one or two records fall to low values while others remain at elevated values. We did not attempt to classify cloud types based estimates of γ . We then defined a threshold and identified periods during which *all* γ values fell below this value. The threshold was determined iteratively by examining PO images at various γ levels and identifying the level that yielded the best likelihood of clear-sky conditions at the OSMOSIS mooring site.

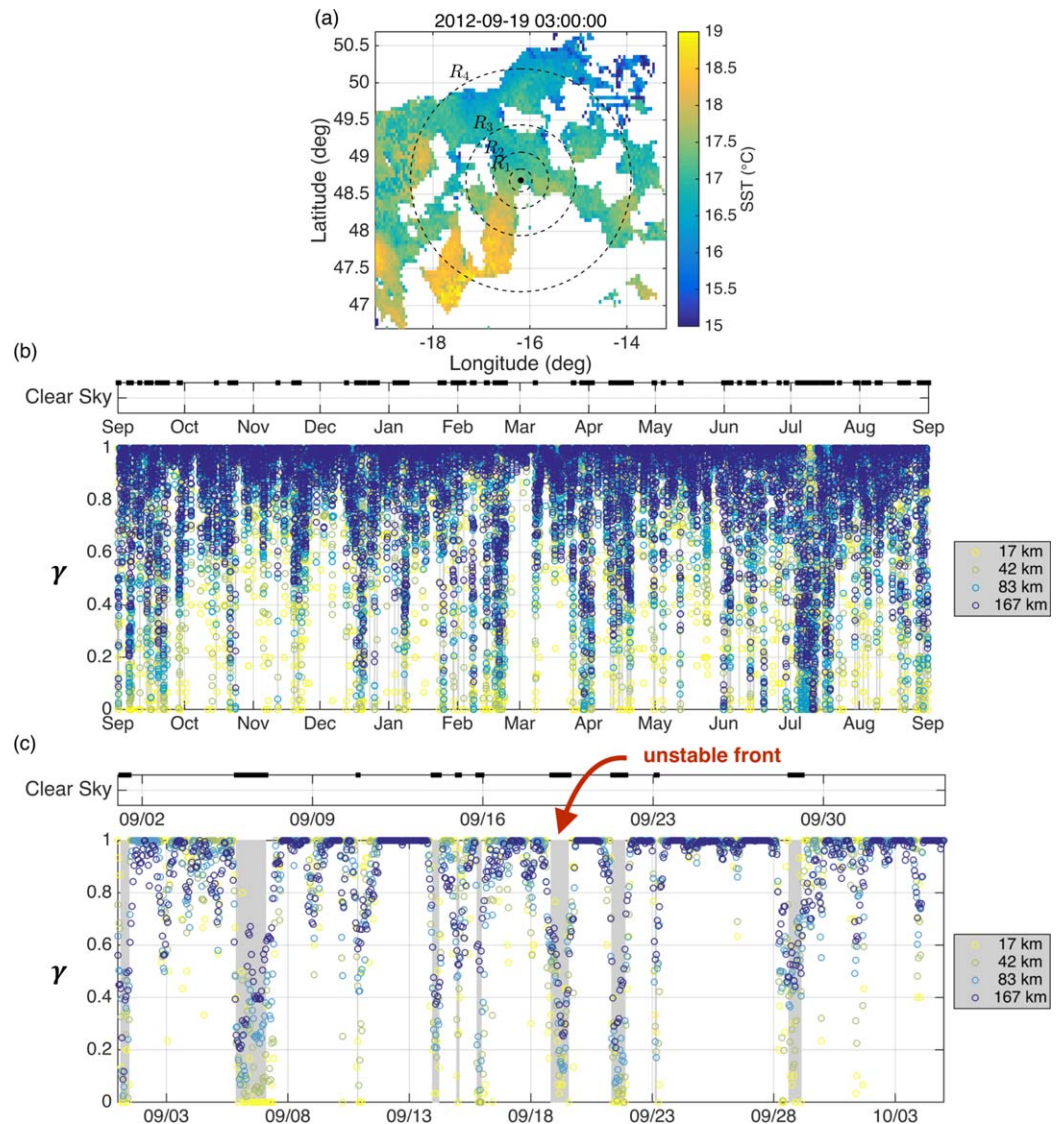


Figure 2. Identification of clear-sky occurrences over the OSMOSIS site (48.69°N, 16.19°W): (a) SST from SEVIRI on MSG-3 valid at the time of the unstable front. Fractional cloud cover, γ , was computed as the fraction of cloud-contaminated pixels within circles of increasing distance from the observation center. (b) Clear-sky occurrences and γ at the OSMOSIS mooring site (2012–2013). (c) Same as Figure 2b but magnified on 1 September to 5 October 2012; clear-sky occurrences are shown in gray and the red arrow highlights the period during which an unstable front was observed (the focus of this study). Colors correspond to radii of small circles, R_1 to R_4 .

We selected 0.6 as our threshold. Having identified instances of low γ , we then cross-referenced these occurrences with available VIIRS data.

We computed γ from near real-time (NRT) data from MSG-3 provided by CERSAT/IFREMER. While we initially used SST generated by the Group for High-Resolution Sea Surface Temperature (GHRSSST) and distributed by the NOAA National Oceanographic Data Center (NODC), this data record was incomplete. To reduce noise in our estimates of γ from the NRT data, we computed γ over 1 h intervals. These data were obtained via file transfer protocol from CERSAT/IFREMER.

2.1.2. Polar-Orbiting Satellite Measurements

The VIIRS sensor provides ocean surface measurements approximately once or twice per day at high spatial resolution [Petrenko *et al.*, 2014]. Brightness temperatures (BTs) are estimated at 390 m resolution, while SST is computed by combining four neighboring BT pixels, resulting in a resolution of 780 m. While we made use of both sensor data, we used VIIRS SST measurements when exploring image quality and, once an image of interest was identified, we subsequently obtained BTs corresponding to these times. The SST and BT data files were obtained from the NOAA Comprehensive Large Array-Data Stewardship System (CLASS, <https://www.class.ngdc.noaa.gov/saa/products/welcome>) and had file sizes of 500 MB and 2 GB. These measurements are contained in the environmental data record (EDR) and scientific data record (SDR), respectively. Note, all data are in swath coordinates.

2.2. In Situ Measurements

In the work that follows, we examine one of the VIIRS BT images in concert with in situ measurements. This particular BT image was taken at a time when the ocean surface mixed layer is relatively shallow (<40 m). Since the moorings resided subsurface and ocean gliders were not functioning properly at this time, we made use of ship-based hydrography in our analysis. By chance, a high-resolution hydrographic survey was conducted at the OSMOSIS site at this time: 19–21 September 2012 [Allen *et al.*, 2013]. This survey made use of a towed, profiling conductivity-temperature-depth (CTD) package known as SeaSoar II [Pollard, 1986] and was conducted to provide context to the moorings. A second survey was conducted but was cut short owing to a passing storm. We focus on the first of these surveys in this study. In conjunction with a ship-mounted acoustic Doppler current profiler (ADCP), these data provide 3-D fields of density and velocity within the top 500 m of the ocean.

We objectively mapped the data [Barnes, 1964, 1994] using an isotropic 10 km smoothing scale to eliminate discontinuities across separate legs of the survey. Note this is approximately 3 times the deformation radius within the mixed layer, $\lambda_d = Nh/f$. (Here f is the Coriolis parameter and N and h are the stratification and effective depth of the surface layer, respectively [Thomas *et al.*, 2008].) We subsequently smoothed vertically using a 5 dbar smoothing scale. This smoothing determines the minimal resolvable scale within our data set and has an adverse effect on our estimates of shear and buoyancy gradients, tending to bias these low. We account for this in our results (also, see supporting information). Absolute velocity was estimated using the geostrophic method [Pond and Pickard, 1983]. We computed dynamic height from the density field, estimated geostrophic velocities and referenced these to velocities measured by a Teledyne/RDI 75-kHz ship-mounted ADCP [Pollard and Regier, 1992]. By comparing ADCP absolute velocity profiles with geostrophic shear estimated from the SeaSoar survey, the best match in shape was obtained at 329 m and deeper. Hence, we used a reference depth of 330 m when calculating absolute geostrophic velocities from the combination of SeaSoar II and ADCP measurements. While this approach approximates the true velocity field under geostrophic balance and, thus, ignores nonlinearities, we estimate moderate values of the gradient Rossby number (0.1–0.5, supporting information). While not small, it provides some justification for this approach. Pressure contours of the interpolated SeaSoar data displayed minimal curvature.

The ADCP measures absolute velocity in the ocean, including both geostrophic and ageostrophic components. As pointed out by one reviewer, this would normally enable quantification of the ageostrophic component of flow by subtracting that component computed above. Within the SBL, vertical motion due to horizontal convergence/divergence is expected to be at its greatest value so we anticipate elevated ageostrophic flow within the SBL. However, while the 75 kHz ADCP is a good-quality instrument, it makes a compromise between vertical resolution in favor of greater vertical extent. The 75 kHz signal sees to depths of 500–800 m. But given a blanking-distance of 25 m and bin-sizes of 16 m, there is approximately only one

independent and good measurement within the SBL. This is unfortunate and we acknowledge this limitation.

3. Results

3.1. Cloud Cover

Figure 2b depicts clear-sky occurrences and γ at the OSMOSIS observation site. To help illustrate how clear-sky occurrences relate to γ computed within different small circles, we magnify a portion of this graphic for September 2012 (Figure 2c). To help with future analysis with the OSMOSIS record, we list in supporting information all periods classified as clear-sky according to our definition and which exceed 2 h in duration.

3.2. Sea Surface Temperature

We manually cross-referenced these periods with the availability of VIIRS imagery, a subset of which we provide as supporting information. A more extensive suite of images is available upon request from the authors. Note that several of the images are degraded by striping, examples of which are found on 21 October 2012 and 8 July 2013. This is a known instrument problem and efforts to reduce its effect on image quality are ongoing [Liu *et al.*, 2013; Bouali and Ignatov, 2014]. Despite these and cloud-related artifacts, the images reveal a complex suite of oceanographic features, one of which is highlighted below.

3.3. Brightness Temperature: The Unstable Front

To help illustrate submesoscale structures within these data, we display in Figure 3 (a) VIIRS SST valid on 19 September 2012 at 03:34 UTC, (b) corresponding BT image but magnified in the vicinity of a thermal front, and (c) altimeter-derived sea surface height (SSH) in the form of sea level anomaly (with respect to a 20 year mean) and associated surface geostrophic velocities. We note that the mean dynamic height is small in this region. The latter gives a sense of scale to those familiar with satellite altimetry. Within the SST image in Figure 3a, vortices of scale 1–10 km are observed on the edge of the thermal front with several swirling vortices to the east that have cyclonic vorticity. An objective estimate of the disturbance scale is provided below. These perturbations in the front are regularly spaced and suggest the front is at the onset of a hydrodynamic instability. To be clear, in the absence of concomitant optics, we cannot say for certain that the underlying phenomena giving rise to these features is the same as spiral eddies [Scully-Power, 1986; Munk *et al.*, 2000; Munk, 2001; Eldevik and Dysthe, 2002]. Nevertheless, objectively identified tracer contours (supporting information) and modelled Lagrangian particle trajectories [Munk *et al.*, 2000; Eldevik and Dysthe, 2002] yield similar structures. So as to distinguish the presently observed eddies from “spiral eddies” seen in optical imagery and make the point that we are using Munk’s work as a springboard for exploring mechanisms giving rise to submesoscale eddies, hereafter we will refer to the observed vortices within the thermal image simply as submesoscale vortices or submesoscale eddies.

3.4. In Situ Hydrographic Observations

In addition to the BT image, we have available coincident in situ measurements. In particular, a hydrographic survey was conducted in this region on 19–21 September 2012 using a towed, profiling CTD package. A portion of the ship track during this survey is overlaid in Figure 3b and the full survey is illustrated schematically in Figure 4a. Here we use these data to provide additional insight into dynamics at the front. The natural reference frame consists of along-front (x) and cross-front (y) coordinates (cf. Figure 3b), with positive values of u and v oriented in these directions, respectively. Cross sections of potential density, ρ_θ , and composite cross sections of potential density and along-front geostrophic velocity, $\overline{\rho_\theta}$ and \overline{u} , are illustrated in Figures 4b–4d. Note composite cross sections were obtained by averaging variables in the along-front direction. This helps to reduce along-front variability and obtain relevant horizontal and vertical views of the front.

The existence of a lateral density gradient in Figures 4b and 4c demonstrates that sharp changes in temperature evident from the satellite image are not compensated by changes in salinity [Rudnick and Ferrari, 1999], in contrast to the front observed by Flament *et al.* [1985]. Additionally, the figure depicts a peak in stratification near 40 m depth and a shallow mixed layer of approximately 25 m. Finally, Figure 4d reveals that the magnitude of horizontal flow is 30 cm s^{-1} , with a considerable fraction of this horizontal flow attributed to the deeper-penetrating mesoscale eddies; the maximum flow \overline{u} associated with the submesoscale front is approximately 5 cm s^{-1} (not shown).

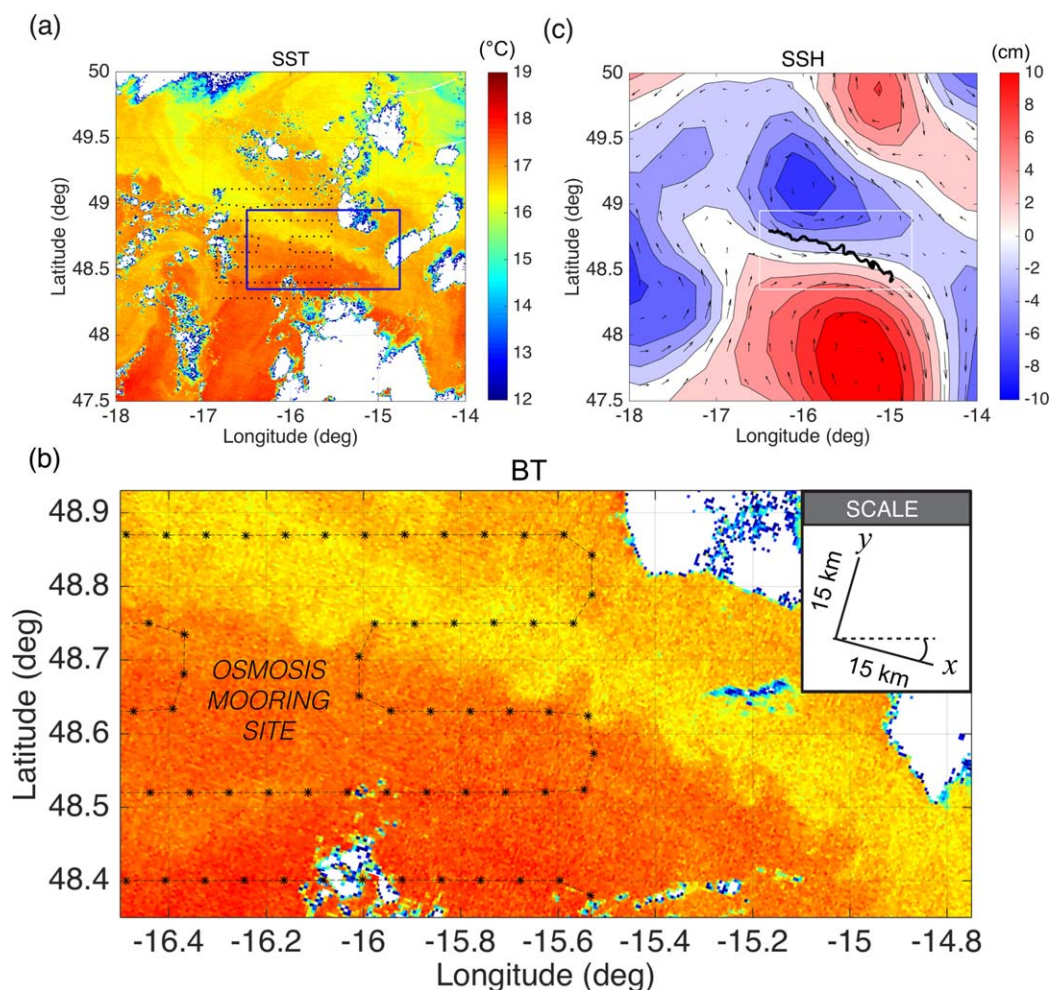


Figure 3. An unstable front in the open ocean: (a) VIIRS sea surface temperature (SST), (b) VIIRS brightness temperature (BT) magnified in the region of the unstable front (valid: 19 September 2012, 03:34 UTC) and (c) sea surface height (SSH) estimated from satellite altimetry and associated surface geostrophic velocities (valid: 19 September 2012). In Figures 3a and 3b, white and neighboring blue (i.e., cool) pixels indicate cloud contamination. In Figure 3b, we indicate the ship track during a high-resolution hydrographic (SeaSoar + ADCP) survey (19–21 September 2012). Asterisks denote profile measurements used in this study. In Figure 3c, the white box indicates the bounding box of the BT image and the black line indicates the frontal edge identified in section 4.2 (cf. Figure A1).

4. Testing Munk's Hypothesis

This provides an ideal case in which we can explore whether barotropic instability (BTI) or baroclinic instability (BCI) gives rise to submesoscale eddies observed on the frontal boundary. The best depiction we have seen of submesoscale eddy generation by a frontal instability is found in *Munk* [2001, Figure 6]. The graphic depicts shear and roll-up of buoyancy contours at subsequent stages of the instability, with cold and warm water located to the north and south of the front, respectively. The onset of the instability occurs at $\tau = 2.5$ days and is principally governed by increased horizontal shear at the northern side of the front. A somewhat analogous graphic based on model simulations of BCI is provided by *Eldevik and Dysthe* [2002, Figure 2]. They show that the onset of instability occurs between $\tau = 2$ days and $\tau = 3$ days, suggesting BCI occurs on a similar time scale. Both illustrations are similar to the observed front examined in this study. In particular, we appear to be seeing the onset of instability immediately before the roll-up of vorticity sheets. This suggests that either BTI or BCI might be giving rise to the vortices.

In speaking of submesoscale eddy formation by BTI, Munk states, "Our hypothesis is based on observational material which consists almost entirely of unrelated glimpses in x, y -space on the sea surface . . . What is required here are prolonged stares or frequent repeat visits coordinated with shipboard observations. We cannot think of any x, y, z, t ocean processes that had been properly identified from measurements in half

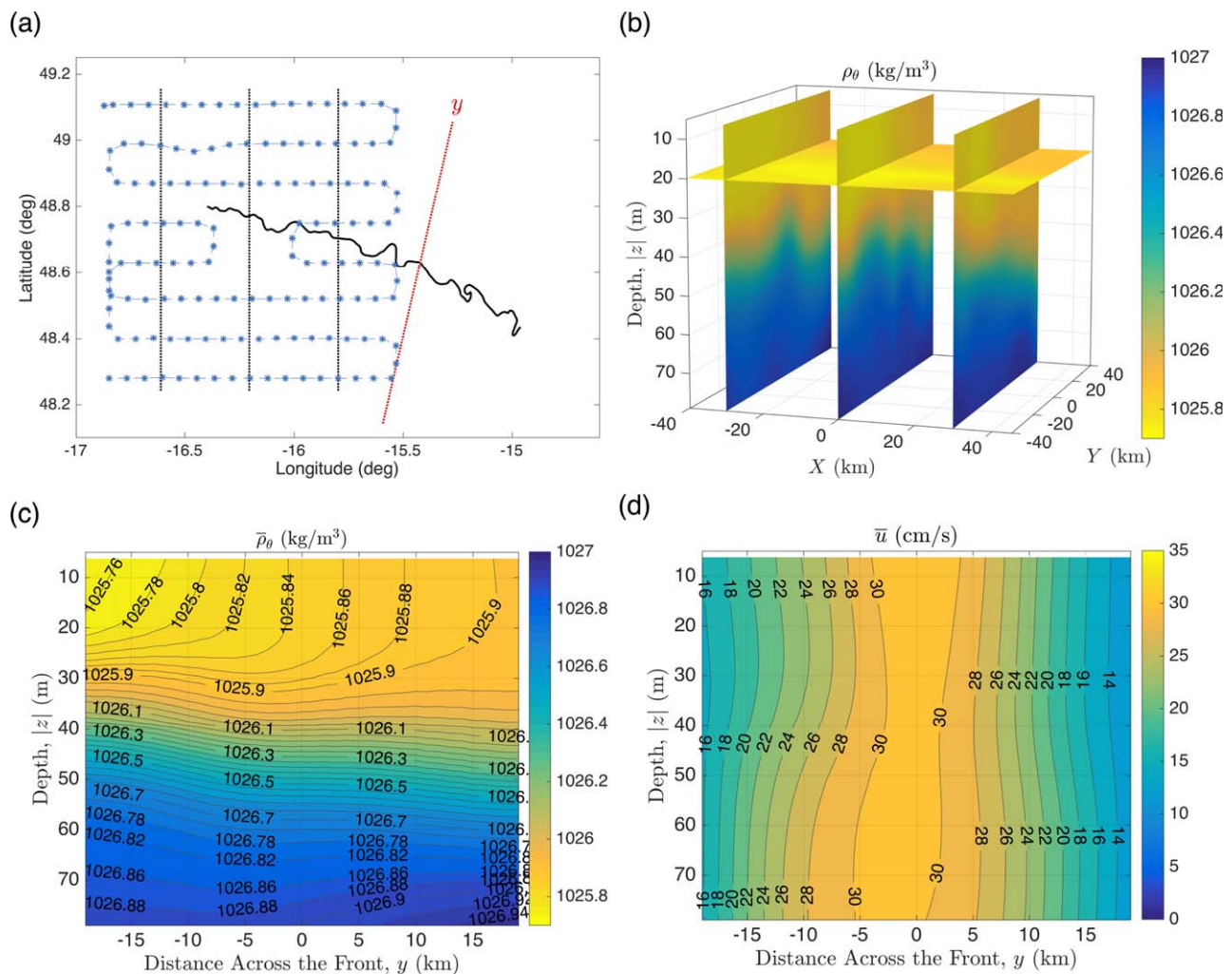


Figure 4. Vertical and horizontal cross sections of potential density and velocity obtained from optimally interpolated SeaSoar II + ADCP hydrography. Figures 4a–4d are as follows: (a) geographic location of SeaSoar measurements (asterisks), cross sections (lines oriented in north-south), and composite cross sections (red line) in the vicinity of the front, (b) potential density, ρ_θ , (c) composite of potential density, $\bar{\rho}_\theta$, and (d) composite of along-front velocity, \bar{u} , centered on the front. In Figure 4b, X and Y are distances in East and North directions, respectively, while in Figures 4c and 4d y is the cross-front distance on which optimally interpolated data are projected (averaged).

the coordinate space" [Munk, 2001]. While the coupled observations presented above do not cover the entire coordinate space—they lack evolution in time t —they nevertheless allow us to determine the underlying formation mechanism giving rise to the submesoscale eddies seen in the satellite image. In particular, the image reveals submesoscale eddies along the edge of the front and we have coincident hydrographic observations describing the horizontal and vertical structure of this front and from which we can estimate relevant oceanographic parameters. We proceed by constructing a hypothesis test, with BTI serving as the null hypothesis and BCI as the alternative. Centrifugal instability [D'Asaro, 1988; Shen and Evans, 2002] is unlikely as gradient Rossby numbers, ζ/f , estimated from the SeaSoar II data are less than unity. We estimate gradient Rossby numbers of 0.1–0.5 (supporting information), with the upper bound being a conservative estimate.

4.1. Overview of the Instability Process

BTI occurs when lateral shear is large. In contrast, BCI occurs when the lateral density gradient or, equivalently, when vertical shear is large [Eliassen, 1983]. While the energy sources for the disturbance differ (i.e., kinetic energy under BTI and potential energy under BCI), in both cases small perturbations to the underlying mean state result in disturbances that grow in time. In special circumstances, the equations can be linearized and simple solutions obtained. Under this approach, one neglects products of perturbations, assumes disturbances of the form $\sim e^{i(kx - \omega t)}$, and solves for the relationship between the complex wave

speed, c and wavenumber k . Here ω is the growth rate of the disturbance. In many cases, the flow can be demonstrated to be most unstable to perturbations characterized by a single wavelength, $2\pi/k$ [Chandrasekhar, 1961; Thorpe, 1971; Drazin and Reid, 1981; Kundu and Cohen, 2008]. See, also, the original work of Lord Rayleigh, Lord Kelvin, and Sir G. I. Taylor. Below, we use these methods in conjunction with the aforementioned observations to investigate what gives rise to the observed submesoscale vortices. As is typical, we assume the observed disturbance remains in its linear growth stage and that the wavelength of the most unstable mode corresponds to twice the diameter of the observed eddies. The hypothesis test is therefore framed in terms of a comparison between observed and theoretically predicted eddy scales. Growth rates cannot be estimated due to considerable cloud cover before and after the event.

A slight inconsistency exists by assuming that the flow is within its linear growth stage and describing the disturbance as consisting of several coherent vortices. That is, on the one hand, we are describing the disturbance as wave-like and on the other, we are describing eddies whose existence necessarily involves non-linearity. This is a fair criticism. However, in the present case we would argue that the satellite image reveals both regular undulations of the frontal boundary and “wispy” vortices, and therefore the linear analysis is merited.

4.2. Observed Eddy Sizes

Observed eddy sizes (i.e., diameters) were estimated from the satellite image in three ways. The rationale for computing these in different ways is that we have little knowledge of the best method for estimating eddy sizes and spread in our estimates provides a measure of observation uncertainty. Methods are described in Appendix A, illustrated in Figure A1 and results are summarized in Table 1. Results of the three methods are consistent and suggest an appropriate eddy diameter is approximately 6 km, with slightly smaller sizes estimated from the radius of curvature method.

4.3. Theoretically Predicted Eddy Sizes

4.3.1. Barotropic Instability

We take as our starting point the Orr-Sommerfeld equation. This equation describes linearized dynamics of parallel shear flow and its derivation from first principles can be found in a number of fluid dynamic texts [e.g., Kundu and Cohen, 2008]. It assumes perturbations of the form $\psi = \phi(y)e^{ik(x-ct)}$, where k is the real-valued horizontal wavenumber, $c = c_r + ic_i$ is the complex phase speed of the disturbance, and $\omega = kc_i$ is the growth rate of the disturbance (i.e., growing if $c_i > 0$). In the limit of infinite Reynolds number (i.e., inviscid flow), the equation governing perturbations to the mean state reduces to the Rayleigh equation: $(u-c)(\phi_{yy} - k^2\phi) - u_{yy}\phi = 0$, where subscripts denote differentiation. Note, the scale of the front is small so that meridional variations in f are negligible when compared with changes in horizontal shear: $|\beta| \ll u_{yy}$. Otherwise, we would concern ourselves with the Rayleigh-Kuo equation [Cushman-Roisin, 1994]. For example, for the observed front, we note a velocity change of U_o over a distance $a = 20$ km. This gives $U_{yy} \sim U_o/a^2 = 6 \times 10^{-10} \text{ m}^{-1} \text{ s}^{-1}$, whereas $\beta = 2\Omega \cos \theta/R_E = 1.5 \times 10^{-11} \text{ m}^{-1} \text{ s}^{-1}$. Here $\theta = 48.5^\circ \text{ N}$ is latitude, $\Omega = 7.292 \times 10^{-5} \text{ s}^{-1}$ is Earth’s angular rotation rate and $R_E = 6371$ km is the mean radius of Earth.

The Rayleigh equation must be solved numerically for arbitrary flows. In special circumstances, however, it can be solved analytically by approximating the observed flow as a linear, piecewise flow [Rayleigh, 1879]. Here we follow this latter approach. The derivation of the analytical solution is detailed in Appendix B. Note: the relevant parameters for this model are the (1) widths of the constant-sheared flow, a and b , on northern and southern sides, respectively, and (2) magnitude of the jet, U_o , above the background velocity.

Table 1. Predicted and Observed Eddy Scales^a

Type	Method	Wavelength (km)	Radius (km)	Diameter (km)
Predicted	Linear BTI	34.2–113.5		17.1–56.7
Predicted	Linear BCI (Eady)	1.4–12.7		0.7–6.3
Predicted	Linear BCI (Stone)	1.5–12.9		0.8–6.5
Observed	Spectra of temperature	11.6, 13.0		5.8, 6.5
Observed	Spectra of frontal boundary	12.0, 13.5		6.0, 6.8
Observed	Radius of curvature		2.3–3.0, 2.6	5.2

^aPredicted scales follow from the BTI and BCI models, while observed scales were estimated using several methods (cf. Figure A1). Eddy diameters are defined as one half the wavelength or twice the radius of curvature. Numbers in bold font correspond to those estimates believed to be more accurate owing to improved wavenumber resolution in spectra.

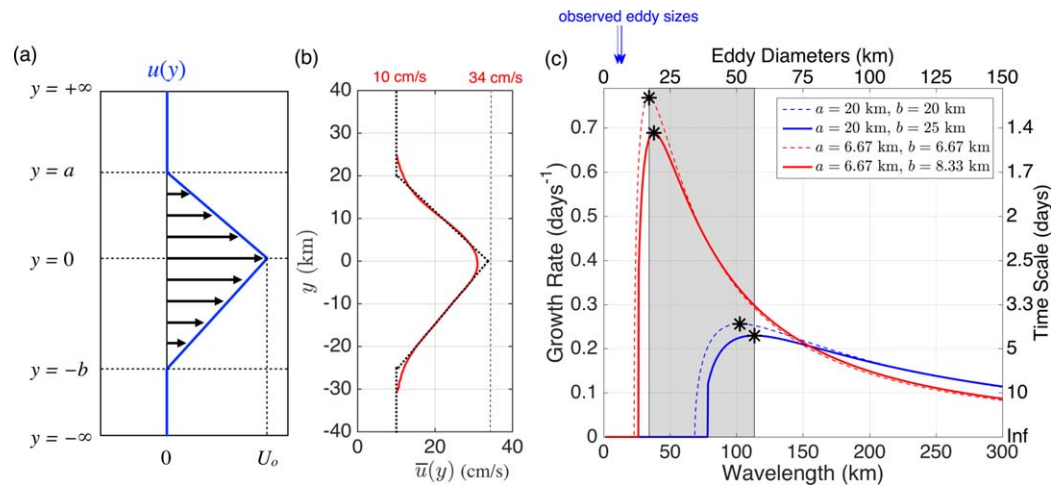


Figure 5. Investigating BTI (null hypothesis) as the governing mechanism: (a) model flow $u(y)$, (b) observed flow $\bar{u}(y)$ derived from the SeaSoar data, and (c) growth rates as a function of horizontal scale for the BTI problem. Here x and u in the along-front direction and y is the cross-front direction. From Figure 5b, we estimate $a = 20$ km, $b = 25$ km, and $U_o = 0.24$ cm s⁻¹. Given smoothing inherent in the SeaSoar data, we conservatively estimate lower bounds on a and b as 6.7 and 8.3 km, respectively (supporting information). These become upper and lower bounds for the instability calculation. For reference, we display growth rate curves corresponding to $a = b$. As the observed eddy diameters (blue arrows, cf. Table 1) fall below our prediction for the most unstable mode (gray region), even when using conservative values for a and b (red lines in Figure 5c), we reject the null hypothesis.

We estimated relevant oceanographic parameters, a , b , and U_o , from the hydrographic data in the following manner. We averaged the observed along-front velocity $u(y)$ in the top 40 m to obtain a representative along-front current, $\bar{u}(y)$ (Figure 5b). We then estimated the width and magnitude of the sheared flow by performing linear regression to northern and southern sides of the front over the intervals $y = \pm[5, 20]$ km (Figure 5b). The maximum current was found to be 0.34 m s⁻¹, and subtracting a background value of 0.10 m s⁻¹ yielded $U_o = 0.24$ m s⁻¹. Given these fits, we specified $a = 20$ km and $b = 25$ km. The ensuing growth rates corresponding to this model are shown in Figure 5c. Finally, we computed growth rates for $a = 6.7$ and $b = 8.3$ km, arguing that the interpolation applied to the SeaSoar measurements smooths the sheared widths by a factor no greater than 3.0 (supporting information). For reference, we also display growth rates when $a = b$ in order to illustrate that results are not very sensitive to slight deviations in a and b .

The growth rates as a function of disturbance wavelength are displayed in Figure 5c. Even using our conservative estimates of a and b , the observed eddy scales are smaller than that predicted by linear BTI; they are outside the gray shaded region in Figure 5c. Formally speaking, we therefore reject the null hypothesis and consider the alternative hypothesis, BCI.

4.3.2. Baroclinic Instability

The frontal model employed here is that of *Eady* [1949]. The model consists of a front in thermal wind balance (i.e., geostrophic and hydrostatic) with mean flow, U , directed in the positive x direction. Superimposed on this mean flow are perturbations with infinitesimal amplitude, $u' \ll U$. While the small scale of the front generally prohibits use of the geostrophic approximation, as mentioned before, the moderate Rossby numbers found here make the approximation somewhat reasonable in our case. We qualify results in the Discussion section. As this model can be found in numerous fluid dynamics texts [Pedlosky, 1987; Cushman-Roisin, 1994; Kundu and Cohen, 2008], we summarize main points in Appendix C but encourage the reader to find the derivation of the most unstable mode in the aforementioned texts.

Applying this model to the observed front is challenging owing to three constraints on the flow. These are (1) dU/dz is constant over a depth H within the upper ocean, (2) N^2 is constant over this same depth, and (3) $w = 0$ at the bottom of this boundary layer. While the first two conditions can be met within the wind- and wave-forced mixed layer and therefore is the most relevant vertical scale for this problem (J. Callies, personal communication, 2016), the latter condition is surely not met owing to low stratification at the base of

the mixed layer and resulting vertical motion. To handle this case, Stone [1966] derived an approximation for the growth rate under conditions of low Ri with the main result being that the solution for the most unstable mode moves to larger wavelengths. Using a different approach, Boccaletti *et al.* [2007] modified the Eady model by allowing a nonzero w for the bottom boundary condition. However, this resulted in a somewhat intractable analytical problem and was solved only numerically. Our approach is instead as follows.

We first note that the baroclinic model presented above with H equal to the mixed layer depth and $w = 0$ at the bottom boundary tends to underestimate the wavelength of the fastest growing disturbance [Boccaletti *et al.*, 2007]. This conveniently provides a lower bound for the wavelength of the most unstable mode. Next, we specify the vertical scale H as the average depth of peak stratification and approximate relevant model parameters by average values within this layer. The argument is that we expect w to be approximately zero at the base of this layer (hereafter, the SBL). This can be rationalized as follows. At the depth of peak stratification, N^2 is large and $\partial\rho/\partial y$ is generally small since it is here that isopycnals converge. Also, thermal wind balance and $du/dz \approx 0$ implies $\partial\rho/\partial y \approx 0$. Assuming density is conserved, $w = g(\rho_o N^2)^{-1}(\partial\rho/\partial t + v\partial\rho/\partial y) \approx g(\rho_o N^2)^{-1}(\partial\rho/\partial t)$. Thus, either $w \approx 0$ or else $\partial\rho/\partial t$ is extremely large, which is unrealistic. (Localized vertical excursions of the pycnocline, or internal waves, can modify this balance through $\partial\rho/\partial t$ and $\partial\rho/\partial y$. However, we argue that BCI essentially is less sensitive to these rapid changes in the pycnocline, being more affected by lower-frequency internal waves but which are associated with smaller w .) Thus, choosing H as depth of peak stratification leads to a more realistic boundary condition and yields an upper bound for the wavelength of the most unstable mode since N and H are overestimated in this manner. In summary, H is chosen as $H_1 =$ mixed layer depth (lower bound) and $H_2 =$ depth of peak stratification (upper bound). Note: we defined the mixed layer depth as the depth at which density is increased an amount 0.01 kg m^{-3} from its value at 8 m depth. This is motivated by work of de Boyer Montégut *et al.* [2004]. Vertical and lateral stratifications are then estimated from average values, $\langle N/f \rangle = N_o/f$ and $\langle M/f \rangle = M_o/f$, within each layer. Here brackets denote averaging in depth and within 5 km of the front. Note from the imaginary part of equation (C3) that lateral buoyancy gradients modify the rate of growing disturbances but do not modify the most unstable mode. We can therefore ignore uncertainty in lateral buoyancy gradients. Also, uncertainty in vertical stratification is dominated by changes in H . The effect of vertical smoothing of the SeaSoar data (i.e., 5 dbar) is negligible when compared with these variations. Thus, uncertainty in our solution is well-captured by the above two bounds. For added information, we also compute the most unstable mode using a depth scale, H_b , defined as the depth scale over which du/dz is constant. Finally we include estimates of the most unstable mode using the approximation of Stone [1966], as well (Appendix C).

Figure 6a displays the relevant parameters of the baroclinic front model. Figure 6b displays the observed parameters within the vicinity of the front. The mixed layer depth H_1 as defined by de Boyer Montégut *et al.* [2004], the depth of peak stratification H_2 and the depth of linear shear H_b are highlighted. Within the SBL, the profile of u falls off approximately linearly over much of the SBL but contains an inflection at deeper depths due to the presence of mesoscale eddies. Also note that M_o/f is approximately constant and nearly equal to $\sqrt{(\overline{d\bar{u}/dz})/f} = 1.72$. Unlike in the Eady and Stone models, however, vertical stratification N/f is not constant with depth.

We approximated relevant model parameters as average values within the aforementioned layers: $N_o/f = [15.5, 70.4, 45.1]$ and $M_o/f = [1.8, 1.6, 1.7]$ corresponding to $H = [H_1, H_2, H_b] = [24, 46, 37]$ m. Figure 6c depicts the growth rates of disturbances given the BCI models presented in Appendix C. The true solution is expected to reside within the gray region. The approximation of Stone [1966] yields similar results, which is attributed to the fact that the front occurs in late summer and the ocean surface is well stratified. (Winds from satellite scatterometry were observed to be low at this time, as well.) As the estimates of observed eddy size nominally reside within the gray region, there is good agreement between the observed eddy diameters and those predicted by linear BCI theory. Deviations are likely caused by constraints in the Eady/Stone models. In conclusion, BCI provides a more plausible explanation for the observed submesoscale eddies. We note that optimal interpolation of hydrographic data tends to bias both U_o (of the BTI model) and $M^2 = -\partial b/\partial y = (dU/dz)f = (U_1/H)f$ (of the BCI model) low. Although this does not change the scale of the most unstable mode—and, thus, does not change the conclusions of this study—it will tend to increase growth rates relative to those depicted here. We mention this with a future modelling study in mind.

4.4. The Existence of Cyclonic Eddies at the Ocean Front

Before concluding the study, we would like to comment on the appearance of cyclonic vortices within the satellite image. This is noted by the swirling eddies toward the right (east) side of the front. Through use of

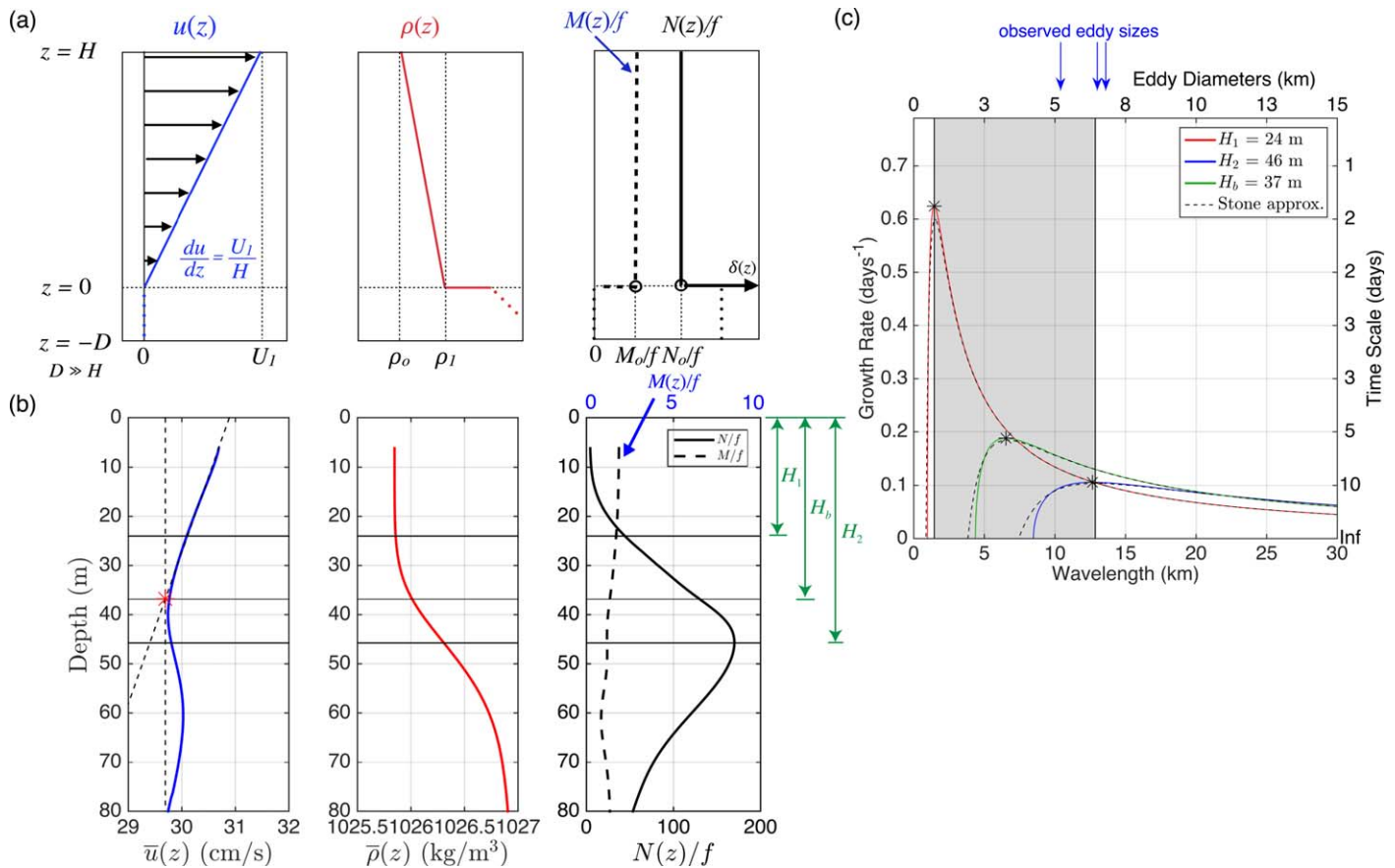


Figure 6. Investigating BCI (alternative hypothesis) as the governing mechanism: (a) model flow and density structure (i.e., constant vertical shear $dU/dz=U_1/H=-M^2/f$ and constant vertical buoyancy gradient N^2), (b) observed flow and density structure, and (c) growth rates as a function of horizontal scale for the Eady (solid) and Stone (dashed) BCI problem. From Figure 6b, we estimate $H_1=24$ m (mixed-layer depth) and $H_2=43$ m (depth of peak stratification). From these we obtain corresponding uncertainty in our estimate of the wavelength of the most unstable mode. We also include our best guess of this wavelength determined from $H_b=37$ m (depth of constant vertical shear). As at least one of the observed eddy diameters (blue arrows, cf. Table 1) fall within our prediction for the most unstable mode (gray region), we “fail to reject” or *accept* this hypothesis. More generally, the observed instability is thought to be the result of both vertical and horizontal shear.

fully nonlinear numerical simulations, *Eldevik and Dysthe* [2002] showed that mixed layer BCI does result in a near-surface portion of the surface mixed layer that is strongly cyclonic, whereas the layer below this is anticyclonic but weakly so. Such asymmetry in the distribution of relative vorticity during BCI can be attributed to conservation of potential vorticity (PV). This is summarized nicely by *Eldevik and Dysthe* [2002] but is explained more fully in Appendix D for the interested reader.

5. Conclusions

Several conclusions can be drawn from the foregoing analysis. First, we conclude that horizontal shear (i.e., BTI) is not the sole mechanism giving rise to the observed eddies within the satellite image. This is evident from a discrepancy between observed and theoretically predicted eddy sizes under linear BTI. This conclusion remains valid even when considering the conservative estimates of a and b , i.e., the widths of the horizontally sheared regions. Second, while we cannot say for certain that mixed layer or submesoscale BCI is the predominant cause owing to large confidence intervals in our calculation of the most unstable mode, the contextual information provided by satellite altimetry, moderate agreement between observed and theoretically predicted eddy sizes, and upper bound on the gradient Rossby number (0.55) all point to BCI as the cause with horizontal shear playing a smaller but influential role. As pointed out by *Eliassen* [1983], all realistic fronts are associated with both mechanisms and it is likely they both play a role at this front.

Assumptions in this study include the following: (i) the frontal instability remains in its linear growth stage and is accurately described by linear dynamics; (ii) hydrographic measurements from SeaSoar II capture sufficiently the relevant gradients at the front; (iii) the analytical models of Rayleigh, Eady, and Stone are applicable; and, relatedly, (iiib) u and b are functions of only one dimension.

The first assumption is reasonable given that the underlying disturbance remains visible and the vortices have not yet separated from the front. Admittedly, nonlinear terms in the horizontal momentum equations are not negligible. We estimate gradient Rossby numbers of magnitude $|\text{Ro}| = |f^{-1} \partial \bar{u} / \partial y| \sim |\zeta| / f = 0.1\text{--}0.5$ (supporting information), with latter values resulting from a conservative estimate of the frontal shear width. Thus, while the geostrophic approximation has been made, we expect frontal intensification and the instability itself [Eldevik and Dysthe, 2002] sharpens buoyancy gradients to the point that this approximation becomes invalid. Such nonlinearities may help explain why observed eddy scales lie nearer the upper bound on the most unstable mode (blue arrows relative to gray region in Figure 6c). Another possibility is that both instability types contribute to the instability, with BTI pushing it to larger scales. With respect to the second assumption, aside from the relaxing of lateral velocity and buoyancy gradients by optimal interpolation, the composite cross sections of velocity u and buoyancy b from the SeaSoar are expected to be representative of the frontal structure. Averaging in the along-front direction smooths out perturbations that may exist in the along-front direction while preserving cross-frontal structure. Nevertheless, the fact that hydrographic measurements are located slightly west of the swirling vortices may introduce inaccuracies in this representation. The third assumption is a challenging one for us. The simple jet-like model of BTI may not be suitable since inflections in the horizontal velocity field may perturb the dynamics of the instability. A similar situation exists in the vertical for the baroclinic case, where inflections in the deeper flow (i.e., 60–70 m depths) due to the mesoscale eddy field might perturb the instability. Furthermore, in contrast to Eady and Stone models, N^2 is not constant below the mixed layer and $w \approx 0$ is questionable at the base of this layer. An exception exists at the depth of peak stratification, H_2 , where we expect $w \approx 0$ except in the presence of internal waves, as discussed earlier. Finally, in contrast to the fourth assumption above, we find that u and b are actually functions of two dimensions, y and z . This results in a more complicated PV structure that must be solved numerically (S. Smith, personal communication, 2017). In summary, the combination of elevated Rossby numbers, slight westward position of the SeaSoar survey with respect to the instability, and limits of validity of these simple models motivate numerical solutions—topics of a future study.

6. Discussion

The frontal instability documented here provides an illustrative example of a forward energy cascade generated by mesoscale frontogenesis. Mesoscale stirring, filamentation, and the onset of BCI leads to a loss of energy that would otherwise proceed up-scale [Batchelor, 1969; Charney, 1971; Rhines, 1979; Müller et al., 2005]. Indeed, this may be one of the reasons why zonal jets predicted from geostrophic turbulence theory are latent in the World Ocean [Maximenko et al., 2008; Berloff et al., 2011; Buckingham and Cornillon, 2013]. One follow-up question, however, is to what extent are these observations representative of observed dynamics in this region? To answer this question, we examined the distribution of lateral buoyancy gradients, M/f , estimated from closely spaced moorings at the OSMOSIS site, September 2012 to September 2013 (Figure 7). As the observed cross-frontal buoyancy gradient, M_o/f , is found within the peak in the probability density function (PDF), we conclude that the observed front is characteristic of fine-scale gradients in this region.

This study suggests BTI and BCI may vary geographically since we expect BTI to vary with the gradient Rossby number. Their relative importance likely varies seasonally, as well. Given the distinction between BTI and BCI in terms of energy pathways and resulting buoyancy fluxes, this has implications for energy and buoyancy budgets in the open ocean. Furthermore, it suggests that circulation patterns and near-surface stratification within ocean models might be improved by incorporating these spatial and seasonal differences. Considerable improvements in ocean stratification have been made by parameterizing mixed layer BCI in climate models [e.g., Fox-Kemper et al., 2011]. However, considerably less attention has been given to energy fluxes. A notable effort to properly represent energy fluxes in a regional model can be found here: <https://www.trr-energytransfers.de/research/area-t/t2/>.

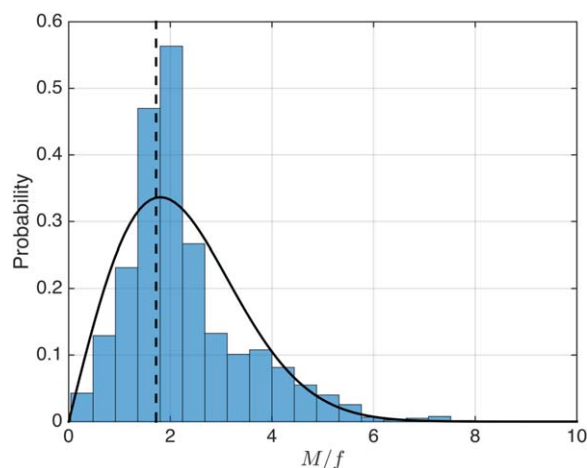


Figure 7. The PDF of lateral buoyancy gradients, $|M/f|$, at the OSMOSIS site, September 2012 to September 2013. Estimates of $|M/f|$ were computed from gradients between moorings spaced approximately 2 km apart. The solid line illustrates a fit to the histogram under an assumption that the PDF follows a Rayleigh distribution. The vertical dashed line denotes the lateral buoyancy gradient, $|M_o/f|$, used in the BCI instability analysis (section 4.3.2). We expect the true value of $|M_o/f|$ is larger by a factor of $\sqrt{2}$.

One of the outcomes of this study is the finding that lateral buoyancy gradients are *at least as important* as horizontal shear in generating small-scale features such as submesoscale eddies in the open ocean. While this conclusion has been known for some time within the modelling community [e.g., Samelson, 1993; Haine and Marshall, 1998; Eldevik and Dysthe, 2002; Boccaletti et al., 2007; Fox-Kemper et al., 2008a, 2008b; Grooms, 2015], corroborating observations in the open ocean are rare. In fact, we believe this is one of the first documented cases of submesoscale BCI in the open ocean. A second outcome of this work is that it identifies a set of in situ observations useful for future studies. Given the paucity of submesoscale observations and expense associated with large-scale field campaigns such as LatMix, OSMOSIS, and SMILES, this is an important result. However, we eagerly await results from the SMILES campaign, particularly as it resides within a

region known for strong turbulent air-sea fluxes and enhanced communication with the deep ocean, i.e., the Southern Ocean.

“Why has the problem received so little attention?” asks Munk in reference to spiral eddy generation. “We assert that the fashion during these years has been statistical rather than phenomenological descriptions of ocean features, and here we are concerned with a truly phenomenological problem” [Munk, 2001]. While not specific to spiral eddies, we believe we provided a platform for further discussion about the relative importance of horizontal and vertical shear in submesoscale eddy generation, a discussion well framed by the work of Munk et al. [2000] and Eldevik and Dysthe [2002]. Moreover, we have demonstrated a method in which observed eddy sizes might be compared with those predicted from various instability mechanisms.

A cautionary note seems appropriate for future readers seeking to apply this method to their observed eddies. The method shown here is fairly unique in that it is applied immediately at the onset of the instability. With increasing time, one must more generally consider the evolution of the eddy in time. In particular, for eddies interacting with each other or other flows, nonlinear triad interactions cause eddies to grow laterally in time owing to inverse energy cascades encountered in 2-D turbulence [Batchelor, 1969; Charney, 1971; Rhines, 1979; Qiu et al., 2008]. This is perhaps more relevant for larger eddies than small, high-Rossby number vortices, as here dissipative effects may become important and counteract such an inverse cascade [Capet et al., 2008; McWilliams, 2016]. In any case, some estimate of the time-since-generation would be an important component of a similar analysis.

Appendix A: Estimating Observed Eddy Sizes

Observed eddy sizes were estimated from the satellite image in three ways. In the first two methods, we estimate this scale from the wavelength of peak power, while in the third method we estimate this scale from the curvature in the front. Each of these methods is described below, illustrated in Figure A1 and resulting eddy scales summarized in Table 1.

A1. Method 1: Spectra of Temperature

In the first method, we identified the peak in the power spectral density (PSD) of temperature obtained along transects of the front. The PSD was computed using both traditional and parametric spectral estimation approaches. The former uses the method of averaged, modified periodograms

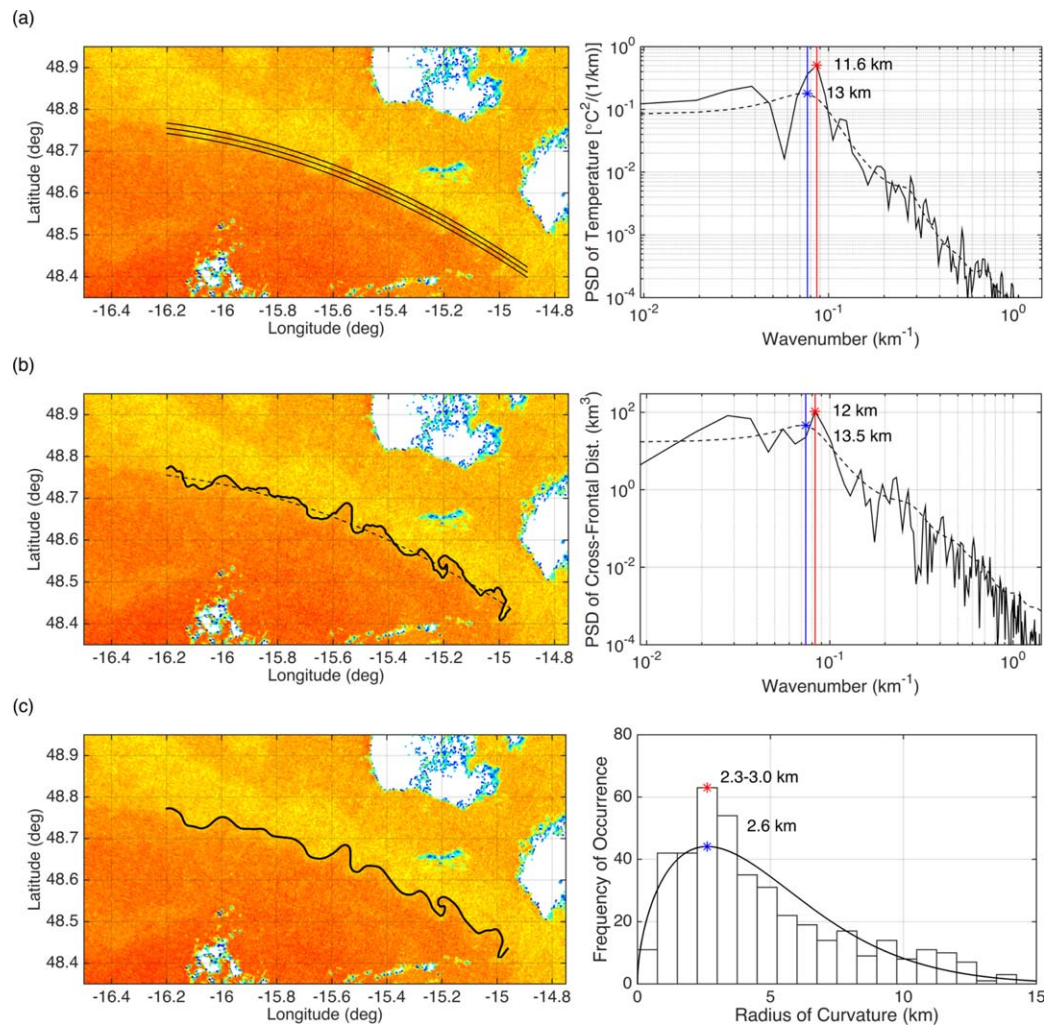


Figure A1. Methods used to estimate observed eddy diameters. In Figures A1a and A1b, we illustrate spectra computed using both traditional (solid) and parametric (dashed) spectral approaches. Asterisks highlight wavelengths corresponding to peaks in the spectral energy. In Figure A1c, we estimated the radius of curvature, $R=|1/\kappa|$, of the frontal boundary, where the boundary was smoothed slightly to improve estimates of curvature. Asterisks highlight the (red) most frequently occurring and (blue) probable radii given a Weibull fit to the data. Eddy diameters were estimated as (a, b) half the peak wavelength and (c) twice the most probable radius of curvature.

[Welch, 1967; Harris, 1978], while the latter models observations as the result of an autoregressive (AR) discrete-time process with $n = 25$ degrees of freedom [Yule, 1927; Walker, 1931]. The advantage of the AR approach is that wavenumber resolution does not depend upon the length of the record [Kay and Marple, 1981]. Eddy diameters are estimated as half the wavelength of peak power (Figure A1a).

A2. Method 2: Spectra of the Frontal Boundary

In the second method, we identified the peak in the PSD of displacements of the frontal boundary, again, using both spectral approaches. In order to isolate the frontal boundary, we used a population-based front detection algorithm described in both Cayula and Cornillon [1992] and Buckingham et al. [2014]. The histogram portion of this algorithm operates by identifying two populations from a distribution of temperatures. Surface temperatures categorized as falling within “cool” and “warm” populations were identified. The resulting binary image was then processed using morphological operations [Gonzalez et al., 2004] and the boundary separating the two temperature populations was identified. Again, eddy diameters are estimated as half the wavelength of peak power (Figure A1b).

A3. Method 3: Radius of Curvature

In the third method, we estimated the radius of curvature of the frontal boundary and identified its most frequently occurring value. The radius of curvature is given by $R=|1/\kappa|$, where

$$\kappa = \frac{\dot{x}\ddot{y} - \dot{y}\ddot{x}}{(\dot{x}^2 + \dot{y}^2)^{3/2}} \quad (\text{A1})$$

is the curvature, and \dot{x} , \dot{y} , \ddot{x} , and \ddot{y} denote first and second derivatives of zonal and meridional displacements with respect to distance along the boundary, s (e.g., $\dot{x}=dx/ds$). This expression was evaluated in its discrete form using first and second differences. We then identified the most probable value of R . While this was done using both a histogram and a PDF-fit to the observed radii. The fit reduces the dependence on bin size when estimating this value from a histogram. (The radius, $R = (x^2 + y^2)^{1/2}$, follows a Rayleigh distribution if zonal and meridional boundary displacements of the frontal boundary, x and y , are normally distributed random variables. We used the Weibull distribution, which is a generalization of the Rayleigh distribution that handles nonnormally distributed random variables.) The eddy diameter was estimated as twice the most probable radius of curvature (Figure A1c).

Appendix B: Linear Barotropic Front Model (Piecewise-Continuous or Rayleigh Model)

B1. Basic State

We model the horizontal shear on the northern side of the front as constant over a distance a and zero as north of this. Similarly, the shear on the southern side is constant over a distance b and zero south of this. A simple expression for the mean flow is therefore $\mathbf{u}=(u, v, w)=(u(y), 0, 0)$, where

$$u(y) = \begin{cases} 0, & \text{if } y \geq a \\ -(U_o/a)(y-a), & \text{if } 0 \leq y < a \\ (U_o/b)(y+b), & \text{if } -b \leq y < 0 \\ 0, & \text{if } y < -b. \end{cases} \quad (\text{B1})$$

The idealized and observed flows are illustrated in Figures 5a and 5b, respectively.

B2. Dispersion Relation

Neglecting perturbations in the vertical (Squires' theorem states that for every 3-D disturbance there exists a 2-D disturbance that is more unstable, such that we need only consider u' and v'), we then introduce a perturbation streamfunction ψ , where $u'=\partial\psi/\partial y$ and $v'=-\partial\psi/\partial x$. Again, assuming disturbances of the form, $\psi=\phi(y)e^{ik(x-ct)}$, the Rayleigh equation applies and has solutions of the form $\phi(y)=Ae^{ky}+Be^{-ky}$, where A and B are arbitrary constants. We additionally require that disturbances are negligible with distance from the front (i.e., $\phi \rightarrow 0$ as $y \rightarrow \pm\infty$) such that the general solution is

$$\phi(y) = \begin{cases} Ae^{-k(y-a)}, & \text{if } y > a \\ Be^{-k(y-a)} + Ce^{ky}, & \text{if } 0 < y < a \\ De^{-ky} + Ee^{k(y+b)}, & \text{if } -b < y < 0 \\ Fe^{k(y+b)}, & \text{if } y < -b. \end{cases} \quad (\text{B2})$$

There are interfacial conditions that must be satisfied at each interface in order for the Rayleigh equation to hold. These so-called "jump conditions" include (1) continuity of pressure and (2) continuity of normal velocity across each interface, and can be expressed as follows:

$$\left[(u-c)\phi_y - \phi u_y \right]_{y=y_o^-}^{y=y_o^+} = 0, \quad (\text{B3})$$

$$\left[\frac{\phi}{u-c} \right]_{y=y_o^-}^{y=y_o^+} = 0. \quad (\text{B4})$$

Here the superscript notation denotes taking the limit as y approaches $y_0 = (a, 0, -b)$ from either side of y_0 . In other words, the expression in brackets is evaluated at either side of the interface and the difference must be zero.

For each interface or discontinuity, jump conditions (5) and (6) provide two equations. As we have three interfaces and as the Rayleigh equation is linear, we have a linear system of six equations and six unknowns (coefficients A through F). This is expressed in vector form as $\mathbf{Ax}=0$, where

$$\mathbf{A} = \begin{bmatrix} kc & -(kc+U_o/a) & (kc-U_o/a)e^{ka} & 0 & 0 & 0 \\ -c^{-1} & c^{-1} & (c^{-1})e^{ka} & 0 & 0 & 0 \\ 0 & (-U_o k + kc + U_o/a) & (U_o k - kc + U_o/a) & (U_o k - kc + U_o/b) & (-U_o k + kc + U_o/b)e^{kb} & 0 \\ 0 & (U_o - c)^{-1}e^{ka} & (U_o - c)^{-1} & -(U_o - c)^{-1} & (U_o - c)^{-1}(-e^{kb}) & 0 \\ 0 & 0 & 0 & (kc - U_o/b)e^{kb} & (-kc - U_o/b) & kc \\ 0 & 0 & 0 & (c^{-1})(-e^{kb}) & -c^{-1} & c^{-1} \end{bmatrix},$$

and $\mathbf{x} = [A, B, C, D, E, F]^T$. For nontrivial solutions, the determinant of \mathbf{A} must be zero. Thus, we set the determinant of \mathbf{A} equal to zero and solve for c . The resulting expression, or dispersion relationship, is a complicated polynomial in c ,

$$\begin{aligned} & (8a^2b^2k^3e^{2ak+2bk})c^3 - (8U_oa^2b^2k^3e^{2ak+2bk})c^2 + 2U_o^2(a^2ke^{2ak} + b^2ke^{2bk} - abk - a^2ke^{2ak+2bk} - b^2ke^{2ak+2bk} + \\ & abke^{2ak} + abke^{2bk} + 2ab^2k^2e^{2ak+2bk} + 2a^2bk^2e^{2ak+2bk} - abke^{2ak+2bk})c + \\ & (U_o^3a + U_o^3b - U_o^3ae^{2ak} - U_o^3ae^{2bk} - U_o^3be^{2ak} - U_o^3be^{2bk} + U_o^3ae^{2ak+2bk} + U_o^3be^{2ak+2bk} + 2U_o^3abk - 2U_o^3abke^{2ak+2bk}) = 0. \end{aligned} \quad (B5)$$

For the case of $b = a$, the expression simplifies to

$$\begin{aligned} & (8a^3k^3e^{4ak})c^3 + (-8U_oa^3k^3e^{4ak})c^2 + (8U_o^2a^2k^2e^{4ak} - 2U_o^2ak + 8U_o^2ake^{2ak} - 6U_o^2ake^{4ak})c + \\ & (2U_o^3e^{4ak} - 4U_o^3e^{2ak} + 2U_o^3 + 2U_o^3ak - 2U_o^3ake^{4ak}) = 0, \end{aligned} \quad (B6)$$

and as it is a cubic, it has three roots. The first is real; the second has a negative imaginary part; and the third has a positive imaginary part and is therefore our solution,

$$c = \frac{U_o}{4ak} \left[2ak - (1 - e^{-2ak}) + e^{-2ak} (9e^{4ak} - 10e^{2ak} + 4a^2k^2e^{4ak} - 4ake^{2ak} - 12ake^{4ak} + 1)^{1/2} \right]. \quad (B7)$$

The imaginary part provides the growth rate of the disturbance, kc_i , as a function of horizontal wavenumber k for specific U_o and a . Note that U_o affects the rate of the growing disturbance but does not determine the most unstable wavelength, as it is outside the square root in equation (B7). More generally, however, we solve the full polynomial expression with arbitrary a and b using a symbolic mathematics software package. We find that the two solutions yield similar growth rates but report both answers for completeness.

Appendix C: Linear Baroclinic Front Model (Eady and Stone Models)

C1. Basic State

The model consists of a front in thermal wind balance (i.e., geostrophic and hydrostatic) with mean flow, $u = U$, directed in the positive x direction. Superimposed on this mean flow are perturbations with infinitesimal amplitude, $u' \ll U$, where the total flow is $u = u' + U$. In addition, we make the following simplifications:

1. The flow is inviscid.
2. The boundary layer thickness, H , is constant.
3. The vertical stratification, $N^2 = \partial b / \partial z$, is constant.
4. The lateral stratification, $M^2 = -\partial b / \partial y = f \partial U / \partial z$, is constant.
5. The vertical velocity, w , is much smaller than the horizontal velocity at all times.
6. $w = 0$ at the bottom and top of the layer ($z=0, H$).

As in the BTI case, we neglect meridional variations in Coriolis. In the above expressions, $b = -g\rho_0/\rho_o$ is the buoyancy of the fluid, g is gravity, and ρ_o is a reference density. The assumption of constant M^2 implies a vertical shear independent of depth: $\partial U/\partial z = U_1/H$. Also, note that $U(x, y, z) = U(z)$. Finally, the statement that $w \ll u, v$ allows us to neglect vertical velocity in the mean but it is essential in the perturbation (i.e., $w = w'$). That is, in order for BCI to occur, we must have nonzero w' between the two boundaries.

C2. Dispersion Relation

The equation governing perturbations from the mean state can be found in a number of fluid dynamics texts [e.g., Pedlosky, 1987; Cushman-Roisin, 1994; Kundu and Cohen, 2008]. For this reason, we simply present the end result. Starting with the linearized quasi-geostrophic (QG) potential vorticity (PV) equation, making the above assumptions and introducing a streamfunction (or pressure) perturbation of the form $\psi = \Psi(z)e^{ik(x-ct)}$, one obtains the following differential equation: $\Psi_{zz} - \alpha^2\Psi = 0$, where $\alpha^2 = N^2k^2/f^2$ represents a stretched horizontal wavenumber squared. Together with boundary conditions, this Sturm-Liouville equation represents an eigenvalue problem. Again, k is the real-valued horizontal wavenumber, $c = c_r + ic_i$ is the complex phase speed of the disturbance. This second-order differential equation has the general solution $\Psi = Ae^{\alpha z} + Be^{-\alpha z}$, where coefficients A and B are determined from boundary conditions, $w = 0$ at $z = 0, H$. Expressed in terms of the perturbation ψ , this gives

$$\left(\frac{\partial}{\partial t} + U\frac{\partial}{\partial x}\right)\frac{\partial\psi}{\partial z} - \frac{dU}{dz}\frac{\partial\psi}{\partial x} = 0, \tag{C1}$$

or, substituting in our expression for ψ ,

$$\left(c - \frac{U_1}{H}z\right)\frac{\partial\Psi}{\partial z} + \frac{U_1}{H}\Psi = 0. \tag{C2}$$

For nontrivial solutions, this—in combination with boundary conditions $w' = 0$ at $z = 0, H$ but expressed in terms of Ψ —yields an expression for the wave speed as a function of horizontal wavenumber,

$$c = \frac{U_1}{2} \pm (f/k) \left[\frac{1}{\text{Ri}} \left(\frac{\alpha H}{2} - \tanh \frac{\alpha H}{2} \right) \left(\frac{\alpha H}{2} - \coth \frac{\alpha H}{2} \right) \right]^{1/2}, \tag{C3}$$

where $\text{Ri} = N^2H^2/U_1^2 = f^2N^2/M^4$ is the gradient Richardson number under thermal wind balance (often referred to as the balanced Richardson number). Disturbances will grow unbounded only if $c_i > 0$. It is straightforward to show that the fastest growing disturbance has wavelength $\approx 3.9NH/f = 3.9\lambda_d$. Strictly speaking, equation (C3) is valid only for $\text{Ri} \gg 1$. Stone [1966, 1970] derived an expression for the growth rate under conditions of low Ri. In terms of wave speed, this expression becomes [Fox-Kemper et al., 2011]

$$c_i = \frac{U_1}{2\sqrt{3}} \left[1 - \frac{2}{15} \frac{k^2 U_1^2}{f^2} (1 + \text{Ri}) \right]. \tag{C4}$$

We compared Stone's approximation with the imaginary part of equation (C3) and find they yield only slight changes in growth rates and wavelengths for the most unstable mode. These effects on wavelength are summarized in Table 1.

Appendix D: On the Prevalence of Cyclonic Eddies at Baroclinic Fronts

A hallmark of submesoscale flows is the prevalence of cyclonic versus anticyclonic eddy flows. While explained elsewhere [e.g., Eldevik and Dysthe, 2002], this skewness in the distribution of relative vorticity can be understood as follows. In this discussion, note the importance of the lateral buoyancy gradient in skewing the distribution of ζ/f .

A fluid parcel with initially zero relative vorticity is generally characterized by positive and negative potential vorticity (PV) in northern and southern hemispheres, respectively. This occurs because of Earth's rotation. For example, for a fluid parcel in the northern hemisphere, (i) in the absence of lateral buoyancy gradients and (ii) for stable stratification, one can show that the Ertel PV is positive: $q = (f + \zeta)N^2 + \omega_h \cdot \nabla b = fN^2 > 0$. Furthermore, in the absence of diabatic and frictional forces, conservation of PV (i.e., $Dq/Dt = 0$) requires q

remain positive or negative in each hemisphere, respectively. These constraints are conveniently summarized in a single constraint by multiplying by the Coriolis parameter: $f q > 0$. For fluid at a baroclinic front, the lateral buoyancy gradient must be considered. Here we use thermal wind balance, as it provides a useful pedagogical tool for understanding the impact of lateral buoyancy gradients on Ro .

For a fluid parcel in thermal wind balance, i.e., $\partial \mathbf{u}_h / \partial z = (-\partial b / \partial y, \partial b / \partial x) / f$, the above constraint simplifies as follows: $f q > 0 \Rightarrow f[(f + \zeta)N^2 + \omega_h \cdot \nabla b] > 0 \Rightarrow f^2(1 + Ro)N^2 - f^2 \|\partial \mathbf{u}_h / \partial z\|^2 > 0 \Rightarrow 1 + Ro - Ri^{-1} > 0 \Rightarrow Ro > -1 + Ri^{-1}$, where $Ro = \zeta / f$ is the gradient Rossby number and $Ri^{-1} = \|\partial \mathbf{u}_h / \partial z\|^2 / N^2 = \|\nabla b\|^2 / (f^2 N^2)$ is the inverse gradient Richardson number for balanced flow. In other words, relative vorticity is constrained both by its value in relation to f and the ratio of vertical and lateral buoyancy gradients.

Physically, what is taking place is that stretching/compression of fluid parcels induces relative vorticity which is unbounded in one direction but which is bounded by Earth's rotation in the other. Lateral and vertical gradients in buoyancy modify the lower bound on Ro by tilting the vortex vector from a vertical direction to one which is slightly horizontal. *Buckingham et al.* [2016] discusses the seasonality of this lower bound on Ro . They found that vorticity was positively skewed within the SBL during winter, but less so outside of this season owing to seasonal changes in the gradient Richardson number. It is also notable that almost all of the observations depicting vorticity skewness have been made during winter [Rudnick, 2001; Shcherbina et al., 2013]. At any rate, because Ro is larger at the submesoscale and Ri is smaller in the upper ocean relative to QG flows, a greater number of cyclonic than anticyclonic eddies are observed at the submesoscale. Applied to the case of BCI, the stretching and compression of fluid columns that occurs during baroclinic instability preferentially selects cyclonic vortices as a result of PV-conservation. We refer the reader to *Eldevik and Dysthe* [2002, Figure 7].

Acknowledgments

We wish to thank the Editor and two reviewers for superb feedback. We are grateful to P. Cornillon, S. Saux Picart, and H. Roquet for help locating NRT MSG-3 SST measurements. We also thank J. Vasquez, T. McKnight, and E. Maturi for discussions regarding data dropouts in MSG-2 data. We thank L. Brannigan and N. Lucas for access to processed ADCP measurements. We thank D. Mountfield of NMF for discussions regarding SeaSoar. Finally, the following individuals provided helpful feedback: S. Henson, Y. Firing, J. Callies, M. Bell, K. Nicholls, S. Griffies, S. Smith, J. Taylor, and D. Whitt. C.B. would also like to thank G. Roullet and colleagues for conversations in Brest, France (November 2015) and S. Belcher for encouragement to work on this project. We would like to specifically acknowledge the contributions of Z.K. His efforts to obtain the satellite imagery and initial analysis during his MSc paved the way for this and subsequent studies. C.B. and Z.K. conducted the linear instability analysis and wrote much of the manuscript. A.M. and J.A. collected, processed, and analyzed the SeaSoar II data. All other authors contributed to ideas central to the manuscript and helped frame the study. Lastly, we congratulate Walter Munk on 100 years. Amazing. VIIRS data were obtained from NOAA Comprehensive Large Array-Data Stewardship System (CLASS). MSG-03 SST were obtained from CERSAT/IFREMER, and SSH measurements were obtained from AVISO/CNES. SeaSoar II specifications are available from Chelsea Technologies Group (<http://www.chelsea.co.uk>). This research was made possible by grants from the Natural Environment Research Council (NE/I019999/1, NE/I019905/1) and National Science Foundation (NSF-OCE 1155676), support for ZK from the Ministry of Environment and Energy, Maldives, and a small computing grant from the University of Southampton.

References

- Allen, J. T., et al. (2013), Cruise report: RSS Discovery Cruise 381, 14 Sep.–03 Oct. 2012: Ocean surface mixing, ocean sub-mesoscale interaction study (OSMOSIS), technical report, Natl. Oceanogr. Cent., Southampton, Natl. Oceanogr. Cent., Eur. Way, Southampton, U. K.
- Barnes, S. L. (1964), A technique for maximizing details in numerical weather map analysis, *J. Appl. Meteorol.*, *3*(4), 396–409, doi:10.1175/1520-0450(1964)003<0396:ATFMDI>2.0.CO;2.
- Barnes, S. L. (1994), Applications of the Barnes objective analysis scheme: Part II: Improving derivative estimates, *J. Atmos. Oceanic Technol.*, *11*(6), 1449–1458.
- Batchelor, G. K. (1969), Computation of the energy spectrum in homogeneous two-dimensional turbulence, *Phys. Fluids*, *12*, 233–239.
- Bauer, P., et al. (2010), Status of cloud and precipitation assimilation at ECMWF, in *JCSDA-ECMWF Workshop Cloud/Precipitation Assimilation*, European Centre for Medium-Range Weather Forecasting (ECMWF), Reading, U. K.
- Berloff, P., S. Karabasov, J. T. Farrar, and I. Kamenkovich (2011), On latency of multiple zonal jets in the oceans, *J. Fluid Mech.*, *686*, 534–567, doi:10.1017/jfm.2011.345.
- Boccaletti, G., R. Ferrari, and B. Fox-Kemper (2007), Mixed layer instabilities and restratification, *J. Phys. Oceanogr.*, *37*(9), 2228–2250.
- Bouali, M., and A. Ignatov (2014), Adaptive reduction of striping for improved sea surface temperature imagery from Suomi National Polar-Orbiting Partnership (SNPP) Visible Infrared Imaging Radiometer Suite (VIIRS), *J. Atmos. Oceanic Technol.*, *31*(1), 150–163, doi:10.1175/JTECH-D-13-00035.1.
- Brüggemann, N., and C. Eden (2015), Routes to dissipation under different dynamical conditions, *J. Phys. Oceanogr.*, *45*(8), 2149–2168, doi:10.1175/JPO-D-14-0205.1.
- Buckingham, C. E., and P. C. Cornillon (2013), The contribution of eddies to striations in absolute dynamic topography, *J. Geophys. Res. Oceans*, *118*, 448–461, doi:10.1029/2012JC008231.
- Buckingham, C. E., P. C. Cornillon, F. Schloesser, and K. M. Obenour (2014), Global observations of quasi-zonal bands in microwave sea surface temperature, *J. Geophys. Res. Oceans*, *119*, 4840–4866, doi:10.1002/2014JC010088.
- Buckingham, C. E., A. C. Naveira Garabato, A. F. Thompson, L. Brannigan, A. Lazar, D. P. Marshall, A. J. George Nurser, G. Damerell, K. J. Heywood, and S. E. Belcher (2016), Seasonality of submesoscale flows in the ocean surface boundary layer, *Geophys. Res. Lett.*, *43*, 2118–2126, doi:10.1002/2016GL068009.
- Capet, X., J. C. McWilliams, M. J. Molemaker, and A. F. Shchepetkin (2008), Mesoscale to submesoscale transition in the California Current System. Part III: Energy balance and flux, *J. Phys. Oceanogr.*, *38*(10), 2256–2269, doi:10.1175/2008JPO3810.1.
- Cayula, J.-F., and P. Cornillon (1992), Edge detection algorithm for SST images, *J. Atmos. Oceanic Technol.*, *9*(1), 67–80.
- Chandrasekhar, S. (1961), *Hydrodynamic and Hydromagnetic Stability*, Dover, New York.
- Charney, J. G. (1971), Geostrophic turbulence, *J. Atmos. Sci.*, *28*(6), 1087–1095, doi:10.1175/1520-0469(1971)028<1087:GT>2.0.CO;2.
- Cushman-Roisin, B. (1994), *Introduction to Geophysical Fluid Dynamics*, Prentice Hall, Englewood Cliffs, N. J.
- Damerell, G. M., K. J. Heywood, A. F. Thompson, U. Binetti, and J. Kaiser (2016), The vertical structure of upper ocean variability at the Porcupine Abyssal Plain during 2012–2013, *J. Geophys. Res. Oceans*, *121*, 3075–3089, doi:10.1002/2015JC011423.
- D'Asaro, E. A. (1988), Generation of submesoscale vortices: A new mechanism, *J. Geophys. Res.*, *93*(C6), 6685–6693, doi:10.1029/JC093iC06p06685.
- de Boyer Montégut, C., G. Madec, A. S. Fischer, A. Lazar, and D. Iudicone (2004), Mixed layer depth over the global ocean: An examination of profile data and a profile-based climatology, *J. Geophys. Res.*, *109*, C12003, doi:10.1029/2004JC002378.
- Drazin, P., and W. Reid (1981), *Hydrodynamic Stability*, Cambridge Univ. Press, Cambridge, U. K.
- Eady, E. T. (1949), Long waves and cyclone waves, *Tellus, Ser. A*, *1*(3), 33–52.
- Eldevik, T., and K. B. Dysthe (1999), Short frontal waves: Can frontal instabilities generate small scale eddies?, in *Selected Papers of the ISOFPP*, edited by A. Zetsepin and A. Ostrovskii, UNESCO, Pushkin, Russia.
- Eldevik, T., and K. B. Dysthe (2002), Spiral eddies, *J. Phys. Oceanogr.*, *32*(3), 851–869, doi:10.1175/1520-0485(2002)032<0851:SE>2.0.CO;2.

- Eliassen, A. (1983), The Charney-Stern theorem on barotropic-baroclinic instability, *Pure Appl. Geophys.*, 121(3), 563–572, doi:10.1007/BF02590155.
- Flament, P., L. Armi, and L. Washburn (1985), The evolving structure of an upwelling filament, *J. Geophys. Res.*, 90(C6), 11,765–11,778, doi:10.1029/JC090iC06p11765.
- Fox-Kemper, B., G. Danabasoglu, R. Ferrari, and R. W. Hallberg (2008a), Parameterizing submesoscale physics in global climate models, *CLI-VAR Exchanges*, 13(1), 3–5.
- Fox-Kemper, B., R. Ferrari, and R. Hallberg (2008b), Parameterization of mixed layer eddies. Part I: Theory and diagnosis, *J. Phys. Oceanogr.*, 38(6), 1145–1165.
- Fox-Kemper, B., G. Danabasoglu, R. Ferrari, S. Griffies, R. Hallberg, M. Holland, M. Maltrud, S. Peacock, and B. Samuels (2011), Parameterization of mixed layer eddies. iii: Implementation and impact in global ocean climate simulations, *Ocean Modell.*, 39(1–2), 61–78, doi:10.1016/j.ocemod.2010.09.002.
- Gonzalez, R. C., R. E. Woods, and S. L. Eddins (2004), *Digital Image Processing Using MATLAB*, Pearson, Prentice Hall, Upper Saddle River, N. J.
- Grooms, I. (2015), Submesoscale baroclinic instability in the balance equations, *J. Fluid Mech.*, 762, 256–272.
- Gula, J., M. J. Molemaker, and J. C. McWilliams (2016), Topographic generation of submesoscale centrifugal instability and energy dissipation, *Nat. Commun.*, 7, Article 12811, doi:10.1038/ncomms12811.
- Haine, T. W., and J. Marshall (1998), Gravitational, symmetric, and baroclinic instability of the ocean mixed layer, *J. Phys. Oceanogr.*, 28(4), 634–658.
- Harris, F. J. (1978), On the use of windows for harmonic analysis with the discrete Fourier transform, *Proc. IEEE*, 66(1), 51–83.
- Kay, S., and J. Marple (1981), Spectrum analysis: A modern perspective, *Proc. IEEE*, 69(11), 1380–1419, doi:10.1109/PROC.1981.12184.
- Khaleel, Z. (2015), Observing the oceanic submesoscale from space: A case study of mixed layer baroclinic instability, Master's thesis, Univ. of Southampton, European Way, Natl. Oceanogr. Cent., Southampton, U. K.
- Klein, P., and G. Lapeyre (2009), The oceanic vertical pump induced by mesoscale and submesoscale turbulence, *Annu. Rev. Mar. Sci.*, 1(1), 351–375, doi:10.1146/annurev.marine.010908.163704.
- Kundu, P. K., and I. M. Cohen (2008), *Fluid Mechanics*, 4th ed., Elsevier, Oxford, U. K.
- Lévy, M., R. Ferrari, P. J. S. Franks, A. P. Martin, and P. Rivière (2012), Bringing physics to life at the submesoscale, *Geophys. Res. Lett.*, 39, L14602, doi:10.1029/2012GL052756.
- Liu, Q., C. Cao, and F. Weng (2013), Striping in the Suomi NPP VIIRS thermal bands through anisotropic surface reflection, *J. Atmos. Oceanic Technol.*, 30(10), 2478–2487, doi:10.1175/JTECH-D-13-00054.1.
- Mahadevan, A., E. D'Asaro, C. Lee, and M. J. Perry (2012), Eddy-driven stratification initiates North Atlantic spring phytoplankton blooms, *Science*, 337(6090), 54–58.
- Maturi, E., A. Harris, J. Mittaz, C. Merchant, B. Potash, W. Meng, and J. Sapper (2008), NOAA's sea surface temperature products from operational geostationary satellites, *Bull. Am. Meteorol. Soc.*, 89(12), 1877–1888.
- Maximenko, N. A., O. V. Melnichenko, P. P. Niiler, and H. Sasaki (2008), Stationary mesoscale jet-like features in the ocean, *Geophys. Res. Lett.*, 35, L08603, doi:10.1029/2008GL033267.
- McWilliams, J. C. (1985), Submesoscale, coherent vortices in the ocean, *Rev. Geophys.*, 23(2), 165–182, doi:10.1029/RG023i002p0165.
- McWilliams, J. C. (2016), Submesoscale currents in the ocean, *Proc. R. Soc. London A*, 472(2189), 1–32, doi:10.1098/rspa.2016.0117.
- Merchant, C. J., A. R. Harris, E. Maturi, and S. Maccallum (2005), Probabilistic physically based cloud screening of satellite infrared imagery for operational sea surface temperature retrieval, *Q. J. R. Meteorol. Soc.*, 131(611), 2735–2755, doi:10.1256/qj.05.15.
- Müller, P., J. McWilliams, and M. Molemaker (2005), Routes to dissipation in the ocean: The 2D/3D turbulence conundrum, in *Marine Turbulence: Theories, Observations and Models*, edited by H. Baumert, J. Simpson, and J. Sundermann, pp. 397–405, Cambridge University Press, Cambridge, U. K.
- Munk, W. (2001), Spirals on the sea, *Sci. Mar.*, 65(S2), 193–198.
- Munk, W., L. Armi, K. Fischer, and F. Zachariassen (2000), Spirals on the sea, *Proc. R. Soc. London A*, 456, 1217–1280.
- Omand, M. M., E. A. D'Asaro, C. M. Lee, M. J. Perry, N. Briggs, I. Cetinić, and A. Mahadevan (2015), Eddy-driven subduction exports particulate organic carbon from the spring bloom, *Science*, 348, 222–225, doi:10.1126/science.1260062.
- Pearson, B. C., A. L. M. Grant, J. A. Polton, and S. E. Belcher (2015), Langmuir turbulence and surface heating in the ocean surface boundary layer, *J. Phys. Oceanogr.*, 45(12), 2897–2911, doi:10.1175/JPO-D-15-0018.1.
- Pedlosky, J. (1987), *Geophysical Fluid Dynamics*, 2nd ed., 1–710 pp., Springer, New York.
- Petrenko, B., A. Ignatov, Y. Kihai, J. Stroup, and P. Dash (2014), Evaluation and selection of SST regression algorithms for JPSS VIIRS, *J. Geophys. Res. Atmos.*, 119, 4580–4599, doi:10.1002/2013JD020637.
- Pollard, R. (1986), Frontal surveys with a towed profiling conductivity/temperature/depth measurement package (SeaSoar), *Nature*, 323(6087), 433–435.
- Pollard, R. T., and L. A. Regier (1992), Vorticity and vertical circulation at an ocean front, *J. Phys. Oceanogr.*, 22(6), 609–625, doi:10.1175/1520-0485(1992)022<0609:VAVCAA>2.0.CO;2.
- Pond, S., and G. L. Pickard (1983), *Introductory Dynamical Oceanography*, 2nd ed., 1–329 pp., Butterworth-Heinemann, Oxford, U. K.
- Qiu, B., R. B. Scott, and S. Chen (2008), Length-scales of generation and nonlinear evolution of the seasonally-modulated South Pacific Subtropical Countercurrent, *J. Phys. Oceanogr.*, 38, 1515–1528.
- Rayleigh, L. (1879), On the stability and instability of certain fluid motions, *Proc. London Math. Soc.*, s1–11(1), 57–72, doi:10.1112/plms/s1-11.1.57.
- Rhines, P. (1979), Geostrophic turbulence, *Annu. Rev. Fluid Mech.*, 11, 401–441, doi:10.1146/annurev.fl.11.010179.002153.
- Rudnick, D. L. (2001), On the skewness of vorticity in the upper ocean, *Geophys. Res. Lett.*, 28(10), 2045–2048, doi:10.1029/2000GL012265.
- Rudnick, D. L., and R. Ferrari (1999), Compensation of horizontal temperature and salinity gradients in the ocean mixed layer, *Science*, 283(5401), 526–529, doi:10.1126/science.283.5401.526.
- Samelson, R. M. (1993), Linear instability of a mixed-layer front, *J. Geophys. Res.*, 98(C6), 10,195–10,204, doi:10.1029/93JC00457.
- Saunders, R. W., and K. T. Kriebel (1988), An improved method for detecting clear sky and cloudy radiances from AVHRR data, *Int. J. Remote Sens.*, 9(1), 123–150, doi:10.1080/01431168808954841.
- Schloesser, F., P. Cornillon, K. Donohue, B. Boussidi, and E. Iskin (2016), Evaluation of thermosalinograph and VIIRS data for the characterization of near-surface temperature fields, *J. Atmos. Oceanic Technol.*, 33(9), 1843–1858, doi:10.1175/JTECH-D-15-0180.1.
- Scully-Power, P. (1986), Navy oceanographer shuttle observations, STS 41-G mission report, technical report, DTIC Doc., Naval Underwater Systems Center (NUSC), Newport, Rhode Island.
- Shcherbina, A. Y., E. A. D'Asaro, C. M. Lee, J. M. Klymak, M. J. Molemaker, and J. C. McWilliams (2013), Statistics of vertical vorticity, divergence, and strain in a developed submesoscale turbulence field, *Geophys. Res. Lett.*, 40, 4706–4711, doi:10.1002/grl.50919.
- Shcherbina, A. Y., et al. (2015), The latmix summer campaign: Submesoscale stirring in the upper ocean, *Bull. Am. Meteorol. Soc.*, 96(8), 1257–1279, doi:10.1175/BAMS-D-14-00015.1.
- Shen, C. Y., and T. E. Evans (2002), Inertial instability and sea spirals, *Geophys. Res. Lett.*, 29, 2124, doi:10.1029/2002GL015701.

- Stone, P. H. (1966), On non-geostrophic baroclinic stability, *J. Atmos. Sci.*, 23(4), 390–400.
- Stone, P. H. (1970), On non-geostrophic baroclinic stability: Part II, *J. Atmos. Sci.*, 27(5), 721–726, doi:10.1175/1520-0469(1970)027<0721:ONGBSP>2.0.CO;2.
- Thomas, L. N., A. Tandon, and A. Mahadevan (2008), Submesoscale processes and dynamics, in *Ocean Modeling in an Eddy Regime, Geophys. Monogr. Ser.*, vol. 177, edited M. W. Hecht and H. Hasumi, pp. 17–38, AGU, Washington, D. C.
- Thompson, A. F., A. Lazar, C. E. Buckingham, A. C. Naveira Garabato, G. M. Damerell, and K. J. Heywood (2016), Open-ocean submesoscale motions: A full seasonal cycle of mixed layer instabilities from gliders, *J. Phys. Oceanogr.*, 46, 1285–1307, doi:10.1175/JPO-D-15-0170.1.
- Thorpe, S. (1971), Experiments on the instability of stratified shear flows: Miscible fluids, *J. Fluid Mech.*, 46(02), 299–319.
- Walker, G. (1931), On periodicity in series of related terms, *Proc. R. Soc. London Ser. A*, 131, 818, 518–532.
- Welch, P. D. (1967), The use of fast Fourier transform for the estimation of power spectra: A method based on time averaging over short, modified periodograms, *IEEE Trans. Audio Electroacoust.*, 15(2), 70–73.
- Yule, G. U. (1927), On a method of investigating periodicities in disturbed series, with special reference to Wolfer's sunspot numbers, *Philos. Trans. R. Soc. London Ser. A*, 226, 267–298.